

Local segregation versus irradiation effects in high-entropy alloys: Steady-state conditions in a driven system

Leonie Koch, Fredric Granberg, Tobias Brink, Daniel Utt, Karsten Albe, Flyura Djurabekova, and Kai Nordlund

Citation: *Journal of Applied Physics* **122**, 105106 (2017); doi: 10.1063/1.4990950

View online: <http://dx.doi.org/10.1063/1.4990950>

View Table of Contents: <http://aip.scitation.org/toc/jap/122/10>

Published by the *American Institute of Physics*

AIP | Journal of
Applied Physics

Save your money for your research.
It's now **FREE** to publish with us -
no page, color or publication charges apply.

Publish your research in the
Journal of Applied Physics
to claim your place in applied
physics history.

Local segregation versus irradiation effects in high-entropy alloys: Steady-state conditions in a driven system

Leonie Koch,^{1,a)} Fredric Granberg,² Tobias Brink,¹ Daniel Utt,¹ Karsten Albe,¹ Flyura Djurabekova,^{2,3} and Kai Nordlund²

¹*Fachgebiet Materialmodellierung, Institut für Materialwissenschaft, TU Darmstadt, Jovanka-Bontschits-Straße 2, D-64287 Darmstadt, Germany*

²*Department of Physics, University of Helsinki, P.O. Box 43, Helsinki FIN-00014, Finland*

³*Helsinki Institute of Physics, University of Helsinki, P.O. Box 43, Helsinki FIN-00014, Finland*

(Received 19 June 2017; accepted 24 August 2017; published online 11 September 2017)

We study order transitions and defect formation in a model high-entropy alloy (CuNiCoFe) under ion irradiation by means of molecular dynamics simulations. Using a hybrid Monte-Carlo/molecular dynamics scheme, a model alloy is generated which is thermodynamically stabilized by configurational entropy at elevated temperatures, but partly decomposes at lower temperatures by copper precipitation. Both the high-entropy and the multiphase sample are then subjected to simulated particle irradiation. The damage accumulation is analyzed and compared to an elemental Ni reference system. The results reveal that the high-entropy alloy—independent of the initial configuration—installs a certain fraction of short-range order even under particle irradiation. Moreover, the results provide evidence that defect accumulation is reduced in the high-entropy alloy. This is because the reduced mobility of point defects leads to a steady state of defect creation and annihilation. The lattice defects generated by irradiation are shown to act as sinks for Cu segregation. *Published by AIP Publishing.* [<http://dx.doi.org/10.1063/1.4990950>]

I. INTRODUCTION

High-entropy alloys (HEAs) constitute a relatively new class of materials, which have recently attracted considerable attention in the field of high-performance materials.¹ They consist of at least four to five principal elements occurring in an equimolar or near equimolar ratio, such that their fractions do not drop below 5% or exceed 35%.^{2–4} HEAs owe their name mainly to the large contribution of configurational entropy to the Gibbs free energy. It is supposed that the influence of the entropy stabilizes random solid solutions even at lower temperatures.^{5,6} However, mixing enthalpies and the atomic size mismatches between the components decisively contribute to the phase selection criterion at lower temperatures⁴ and the formation of secondary phases can often not be completely avoided.⁷

The interest in high-entropy alloys is mostly triggered by their outstanding mechanical properties, making them alternatives for certain superalloys or metallic glasses.^{2,4,8–16} However, high-entropy alloys are not only characterized by a large configurational entropy, but also by high atomic-level stresses arising from local lattice distortions due to atomic size differences.¹⁷ It has been reported that structural and chemical disorder affects both defect kinetics and heat dissipation, which are of particular interest in the context of radiation resistant materials.¹⁸ Recent molecular dynamics (MD) simulations revealed that defect concentrations can be significantly reduced during irradiation in equiatomic multi-component alloys as compared to elemental metals.^{19,20} This advantageous robustness against radiation damage can be ascribed to a reduced defect mobility and consequently a

smaller growth rate of defect clusters.^{19–21} Additionally, chemical disorder decreases thermal conductivity, which is also assumed to prevent the formation of large defect clusters by facilitating defect annihilation.^{17,18,22} If, on the other hand, a HEA has a tendency towards multiphase formation at lower temperatures, particle irradiation can also drive the system into thermodynamic equilibrium and lead to precipitation.²¹ Thus, in irradiated high-entropy alloys there is a delicate interplay of thermodynamic driving forces due to configurational entropy, mixing/demixing tendencies, and irradiation-induced far-from-equilibrium conditions.

The objective of the present study is to address this issue in a model four-component CuNiCoFe alloy in thermodynamic equilibrium and under particle irradiation, as well as to study the transition from a single phase HEA to a multiphase or so-called compositionally complex alloy. Using a hybrid simulation scheme consisting of alternating Monte-Carlo (MC) and MD steps, we start by generating a model alloy which is truly stabilized by configurational entropy at elevated temperatures. We then show that this structure decomposes at lower temperatures by precipitation of small copper clusters. Both the high-entropy and the partly decomposed samples are then subjected to a series of 1500 recoil events and the damage accumulation is analyzed and compared to elemental Ni as the reference system. Moreover, we show that segregation effects occur at irradiation-induced defects, promoting the formation of precipitates.

II. METHODS

A. Interatomic potential

We chose a CuNiCoFe alloy as a model system for HEAs with a tendency for Cu segregation at low temperatures. The

^{a)}Electronic mail: koch@mm.tu-darmstadt.de

embedded atom method²³ (EAM) was used to describe interatomic interactions in the multicomponent system. Parametrizations for the elemental interactions were taken from Zhou *et al.*²⁴ The missing cross terms were created using the potential generator from the same authors, which is based on a single element mixture procedure.²⁴ Because of the ferromagnetic elements, magnetism and magnetic transitions could influence the evolution of chemical ordering. EAM potentials cannot explicitly capture these effects and include the magnetic energy contributions only implicitly. For this reason, our system can only serve as a model for nonmagnetic HEAs or HEAs without magnetic transitions. In order to nonetheless ensure the reliability of the potential, we validated it against reference data in the [Appendix](#).

B. Equilibrium simulations

Initially, atoms were distributed randomly on a regular FCC lattice of about $N = 100000$ sites, such that an equimolar configuration was obtained. We applied 3-dimensional periodic boundary conditions and the initial lattice constant was approximated according to Vegard's law.²⁵ After the construction of the initial structure, we minimized its free energy with a mixed MC/MD procedure, carried out using the open source code LAMMPS.²⁶ For the MC steps, we used the variance-constrained semi-grand-canonical (VC-SGC) ensemble.²⁷ This ensemble is based on the semi-grand-canonical ensemble with an added constraint on the overall composition. Thus, it resembles a canonical ensemble, but allows Gaussian variations of the concentration, the extent of which is controlled by the parameter κ . We chose a value of $\kappa = 10^3$ in our simulations. The VC-SGC ensemble allows simulations inside miscibility gaps and has a performance advantage over the canonical ensemble, which cannot be parallelized easily.²⁷ The miscibility is controlled via the chemical potential differences. The chemical potential differences with regard to copper were determined as $\Delta\mu_{\text{Cu-Ni}} = 0.9 \text{ eV}$, $\Delta\mu_{\text{Cu-Co}} = 0.85 \text{ eV}$, and $\Delta\mu_{\text{Cu-Fe}} = 0.7 \text{ eV}$ as described in Ref. 28. The values at hand lead to a miscible CuNiCoFe system at 800 K.

The MC/MD simulations were performed at different target temperatures $T = 800 \text{ K}, 750 \text{ K}, \dots, 400 \text{ K}$, with $N/4$ MC trial moves followed by 20 MD steps. For the MD steps, we used a timestep of 1 fs, as well as a Nosé–Hoover thermostat and a Parinello–Rahman barostat at temperature T and ambient pressure. In total, the simulations were run for 1 000 000 MD steps (including 50 000 MC cycles), after which the potential energy was definitely converged.

C. Irradiation simulations

We simulated irradiation of the structures using the approach introduced in Ref. 19 with the PARCAS MD code.^{29,45,75,76} Simulations were started from either pure Ni, a CuNiCoFe cell with random element distribution, or the equilibrated sample from the MC/MD run at 400 K. After equilibration at room temperature to zero pressure, the simulation cell size was fixed and a series of subsequent 5 keV recoils was initiated in the cell. The recoils were performed by assigning a velocity vector with a magnitude

corresponding to the recoil energy and a random direction to the atom closest to the center of the simulation cell. Each recoil was simulated for 30 ps, which was sufficient to cool the cell back down to ambient temperature by Berendsen temperature scaling³⁰ in a thin layer at the simulation box boundaries. After this, all atom coordinates were shifted by a displacement vector with components randomly selected in the interval $[0, L_d]$, where L_d is the cell size in each of the 3 dimensions d . After the shift, atoms outside the boundaries were wrapped back into the cell according to the periodic boundary conditions. This procedure ensures homogeneous irradiation of the entire simulation cell. Experimentally, this is comparable, e.g., to prolonged neutron or high-energy ion irradiation of a segment inside the material.

The irradiation simulations used the same interatomic potential as the MC/MD simulations, except that for small interatomic separations (well below the equilibrium nearest-neighbor distance) the potentials are smoothly joined to the universal repulsive Ziegler–Biersack–Littmark (ZBL) interatomic potential.³¹ The ZBL-96 electronic stopping³² was applied on all atoms with kinetic energies higher than 1 eV. Monitoring of the simulations showed that about 20% of the initial recoil energy was lost to electronic stopping, i.e., the nuclear deposited damage energy per recoil is about 4 keV. The total deposited nuclear energy was extracted by summing up the damage energies and then used to calculate the displacement-per-atom (dpa) value, a standard unit for radiation damage exposure.^{33,34} This irradiation simulation approach has previously been demonstrated to lead to a good agreement with experiments on other HEAs.^{19,35}

D. Analysis of the short-range order and lattice defects

In order to quantify the chemical ordering, we used the Warren–Cowley short-range order (SRO) parameters α_1 and α_2 adapted to a multicomponent alloy³⁶

$$\alpha_n^{ij} = 1 - \frac{P_n^{ij}}{c_j}, \quad (1)$$

where the subscript $n \in \{1, 2, \dots\}$ refers to the n th coordination sphere, P_n^{ij} describes the conditional probability of an atom of type j being adjacent to an atom of type i , and c_j is the concentration of atom type j . A Warren–Cowley parameter of zero represents the case of an ideal solid solution with no tendency for clustering. Ordered structures (attractive SRO) can be assumed if α is positive, while negative values reflect preferences for segregation (repulsive SRO). We calculated the SRO parameters for the equilibrium structures as a time average over 20 snapshots taken during 2000 simulation steps. Those snapshots were minimized prior to analysis to remove thermal fluctuations and to obtain the 0 K ground-state values. For the irradiated cells, the SRO analysis was performed in the same manner, except that averaging was only performed where noted.

We used the open source application OVITO³⁷ for the analysis and visualization of simulation results: Atomic volumes were calculated by Voronoi tessellation of minimized samples,^{38–41} defective atoms were marked by common neighbor analysis (CNA) with an adaptive cutoff,^{42,43} and dislocation

lines were identified using the dislocation extraction algorithm (DXA).⁴⁴ Additionally, we also performed a Wigner–Seitz cell defect analysis.⁴⁵ This analysis constructs the space-filling Wigner–Seitz cells of the perfect underlying FCC lattice, labeling empty cells as vacancies and doubly filled ones as interstitials. Since this analysis is space-filling, it gives a definite determination of whether a defect region is of vacancy or interstitial type (complex defects may involve both, but then the difference in the number of vacancies vs. interstitials of the same cluster determines its character⁴⁶) The [supplementary material](#) provided by this analysis helps to identify point defects, which cannot be treated by DXA.

III. RESULTS AND DISCUSSION

A. CuNiCoFe in thermodynamic equilibrium

Figure 1 shows the final structures after equilibration in the VC-SGC ensemble at 800 K (left) and at 400 K (right). The configurations differ slightly in their atomic arrangement. Whereas Cu (red atom type) appears to be randomly distributed at 800 K, it tends to form small clusters in the structure at 400 K, indicated by the white arrow. The Warren–Cowley parameters at both temperatures are shown in Fig. 2. All α_n values more or less deviate from the ideal solid solution in either the positive or negative direction. This behavior is most pronounced for Cu. On average, we find a Warren–Cowley parameter for Cu–Cu of -0.15 for the first neighbor shell at 800 K, indicating a slight tendency to form small Cu clusters (positive ΔH_{mix}). Accordingly, all other $\alpha_1^{\text{Cu}-j}$ values are positive. Except for Fe–Fe interactions, all remaining parameters are slightly negative, indicating miscibility of Ni, Co, and Fe. The α_2 parameter exhibits no strong indication for medium-range ordering at 800 K.

If we repeat the analysis in the same sample equilibrated at 400 K, we see that the ordering tendencies become more distinct and extend into the second neighbor shell. Although the Warren–Cowley parameters for non-Cu pairs also change in magnitude, they still indicate an approximately random solid solution of Co, Ni, and Fe without any remarkable clustering. This can also be inferred from the snapshots in Fig. 1. Figure 2(c) further shows that the Cu segregation tendencies increase non-linearly with decreasing temperature. Note that we do not observe any structural phase transitions, such as a transition from an FCC to a BCC lattice or even amorphization.

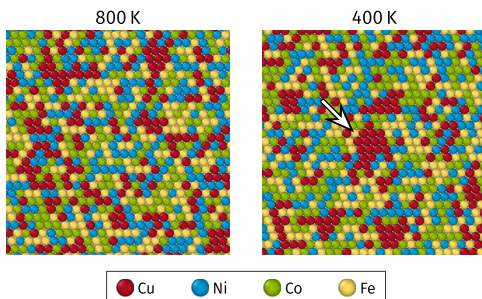


FIG. 1. Snapshots of the CuNiCoFe alloy, equilibrated in the VC-SGC ensemble at 800 K (left) and 400 K (right). The arrow highlights a clustering of copper atoms, indicating that phase separation occurs at lower temperatures.

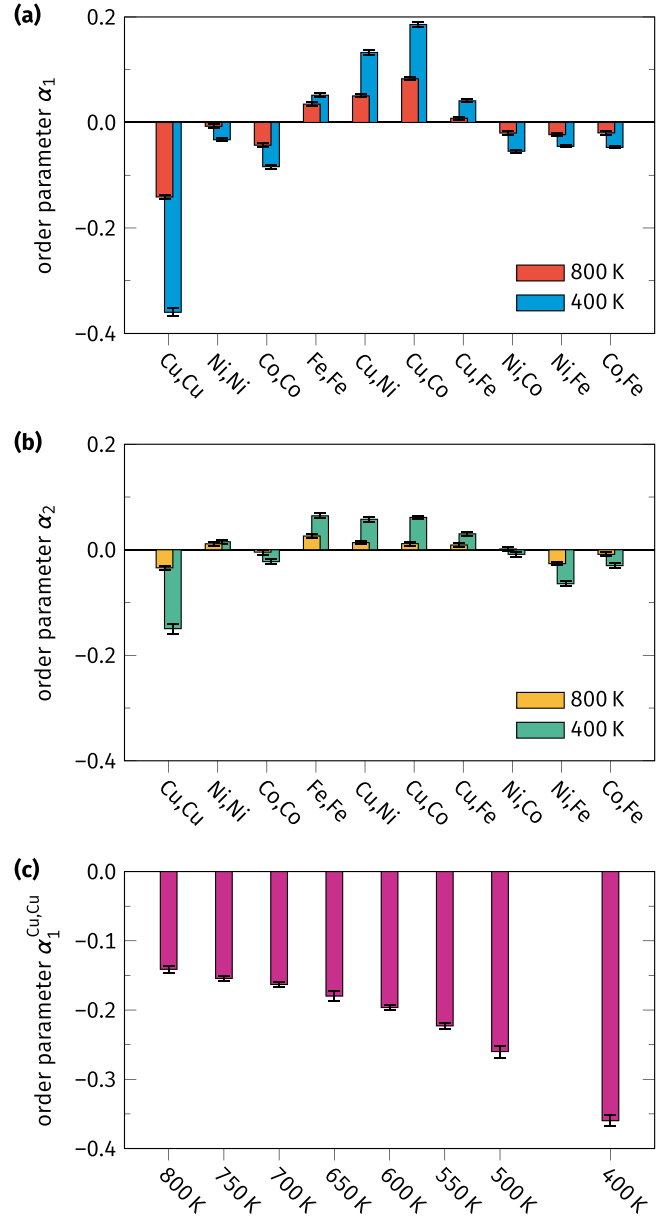


FIG. 2. Warren–Cowley parameters α_1 (a) and α_2 (b) for the CuNiCoFe alloy system at 800 and 400 K. (c) The change of $\alpha_1^{\text{Cu,Cu}}$ with temperature. Increasing Cu–Cu ordering tendencies can be observed with decreasing temperature. All values are averaged over 20 snapshots at 0 K, with the error bars representing the standard deviation.

These results may be interpreted as follows: The contribution of the configurational entropy at 400 K is insufficient to compete against the enthalpy of mixing. Since the composition of the system is fixed, it will demix by locally forming copper-rich clusters. The formation of two separate solid solution phases (Cu-rich and Cu-depleted) has already been confirmed experimentally by Otto *et al.*³ The observed decomposition is more pronounced than in the present simulation, which may either be due to the different composition in the experiment (CoCrFeMnCu), or the higher solubility of Cu in the EAM potential (see [Appendix](#)). The authors found that the Cu segregation is driven by positive binary mixing enthalpies between copper and the remaining components.³ Thus, when decreasing the temperature in the experiment, there is a competition between the increasing thermodynamic driving

force for decomposition and the decreasing diffusivity within the system. For this reason, HEAs often represent kinetically trapped metastable configurations at lower temperatures and local segregation occurs as an ageing phenomenon.

When comparing the atomic volumes as a function of the atom type (see Fig. 3), it can be seen that Cu has slightly larger values than Co, Ni, or Fe. Both Ni and Co possess higher atomic volumes in the multicomponent system than in their elemental state. In contrast, Cu and Fe exhibit smaller atomic volumes compared to their pure structures. At 400 K, the system starts demixing into a ternary Co, Ni, and Fe solid solution and into a copper-rich phase. The copper atoms expand slightly, while the ternary solid solution becomes slightly denser. This brings Cu, Co, and Ni closer to their preferred atomic volume. Only Fe deviates from this trend, but exhibits a positive Warren–Cowley parameter, indicating a preference for unlike neighbors. This changed chemical environment may influence the equilibrium volume.

In summary, these observations suggest that the small scale decomposition is driven largely by the mixing enthalpy at low temperatures, but additionally enhanced by atomic size effects.

B. Irradiation

Thus far, we studied the thermodynamic stability of a CuNiCoFe solid solution. In Sec. III A, we demonstrated by means of hybrid MC/MD simulations that CuNiCoFe exhibits a tendency for decomposition at lower temperatures (400 K). These results suggest that in this case a random distribution is only stabilized by kinetic inhibition. In the following, we will therefore discuss the effect of cascade events on the evolution of the chemical order, focusing on the question, if the energy that is released during recoil events enables the decomposition of Cu. We irradiate both the equilibrated, partially segregated sample obtained by MC/MD simulation at 400 K (“initially

segregated”), and a sample with completely random element distribution (“initially random”). Additionally, we investigate the structural damage due to irradiation by comparison with a Ni sample.

1. Lattice defects

Earlier work comparing irradiation damage in elemental metals and disordered alloys suggests that the FCC structure is retained throughout irradiation with 1500 recoils.¹⁹ Figure 4(a) shows that this is also the case for the initially segregated HEA sample (equilibrated with MC/MD at 400 K). Since the structural damage in the initially random HEA is similar, we omit this sample from the discussion at hand. For comparison, Figure 4(b) shows a pure Ni reference sample which underwent the same irradiation treatment. Most irradiation damage in these samples manifests itself by the formation of dislocation loops, stacking-fault tetrahedra, and single vacancies or vacancy clusters. Vacancy clusters and extended defect agglomerates cannot be identified by the DXA and are indicated by red defect meshes. A visualization of atom positions in Fig. 4(c) reveals that these regions are dominantly characterized by vacant lattice sites. The nature of these regions has also been confirmed by a Wigner–Seitz cell defect analysis, which shows that the positions of the distorted regions generally coincide with vacancy-type defect clusters (see videos *cascade-CuNiCoFe.avi* and *cascade-Ni.avi* in the [supplementary material](#)). These vacancy-type defects are homogeneously distributed within the structure.

The irradiation process and therefore the formation and evolution of defects can be divided into three stages. Figures 4(a) and 4(b) visualize one representative configuration for each of the three stages. Figure 4(d) depicts the defect concentration as a function of the irradiation dose. Initially, the HEA shows a higher defect accumulation than the pure Ni system, which could be caused by higher atomic level stresses within the multicomponent system. This results in a reduced defect formation energy and thus increased number of defects.¹⁷ In turn, pure Ni exhibits a higher recombination rate due to an increased point defect mobility,^{18,22} which means that fewer defects are created per recoil event. During the first cascades, mainly point defects occur in both structures, while the concentration of dislocation-network-like structures is still small.

In the second stage, with an increase of irradiation damage, the defect concentration in pure Ni increases and reaches the same magnitude as in the high-entropy structure. It can be seen that apart from vacancies and stacking-fault tetrahedra, a rather large and stable dislocation loop is formed by the agglomeration of small defects during successive cascades. In general, the rate of defect annihilation depends on both the size and the spatial distribution of the defects. Small defects can be annihilated if they are hit by a single recoil event, while larger defect structures are not engulfed completely and are therefore more stable. Furthermore, the agglomeration of defects in Ni leads to their localization, while the small defects in the HEA are more homogeneously distributed. This means that the probability of a cascade randomly hitting a defect is higher in the HEA and a steady state of annihilation and creation is reached (see video *cascade-CuNiCoFe.avi* in

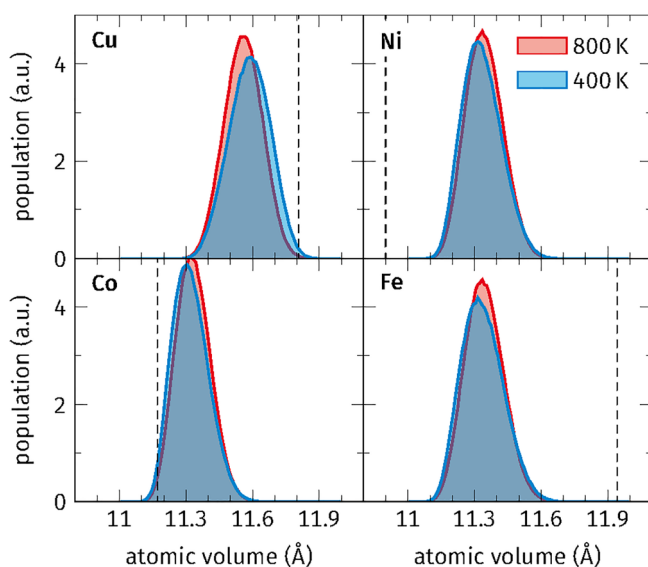


FIG. 3. Histograms of the atomic volumes at 0 K for the HEA equilibrated at 400 K (blue) and 800 K (red). The dashed lines indicate the ground state atomic volume of the single-element FCC structures. Atomic volumes are obtained from Voronoi tessellation^{38–41} of 20 snapshots at 0 K.

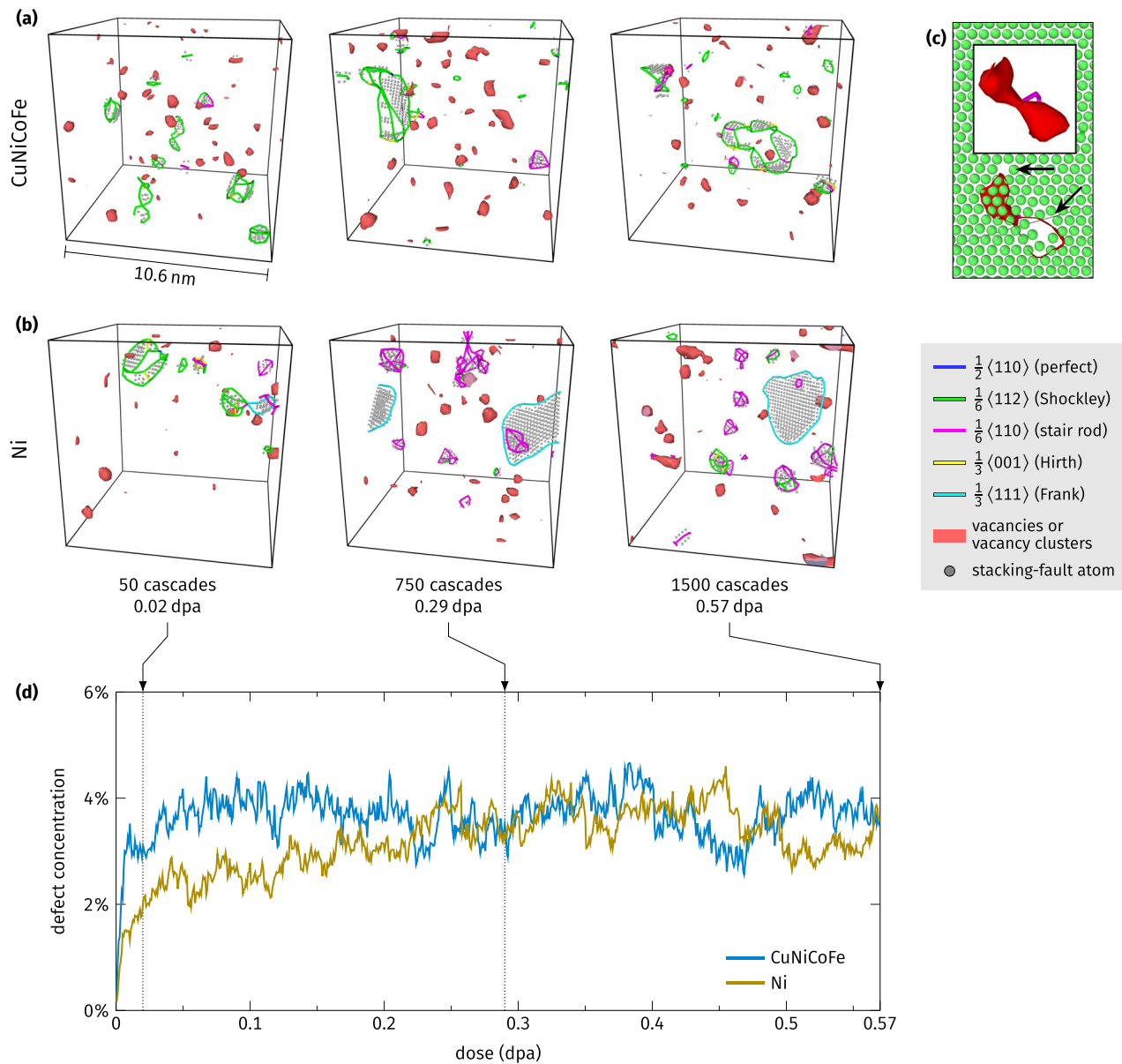


FIG. 4. Analysis of the build-up of lattice defects during irradiation. (a) DXA analysis of the initially segregated HEA at different irradiation doses. (b) The same for a Ni sample. Empty space represents the perfect FCC lattice; the structures do not collapse during irradiation. Green lines indicate $\langle 112 \rangle$ partial dislocations, turquoise lines indicate a Frank loop, purple lines belong to stacking fault tetrahedra, and red surfaces enclose defects that cannot be recognized by DXA. Videos of these simulations can be found in the [supplementary material](#) (CuNiCoFe-ordered-DXA-during-irradiation.avi and Ni-DXA-during-irradiation.avi). (c) A closer look at those red regions reveals that they represent vacancies and vacancy clusters. In (d), a plot of the concentration of defective atoms as identified by CNA is shown as a function of the irradiation dose. In agreement with the DXA results, we can see that the HEA quickly reaches a high defect concentration that saturates around 4%. These defects consist mostly of vacancies and small dislocation networks. Pure Ni builds up the defect concentration more slowly. At first—similar to the HEA—vacancies and small dislocation networks appear, then these start disappearing in favor of stacking-fault tetrahedra and a Frank loop.

the [supplementary material](#)). A small number of stacking-fault tetrahedra appear, but seem to be unstable. Additionally, we can observe the formation of complex networks of partial dislocations. Because of the large amount of dislocation junctions, these networks must be sessile. Thus, large movements of these networks must again be a series of annihilation and creation events, and they are therefore also unstable against irradiation. In Ni, the defects are assimilated into larger structures, such as sessile Frank dislocation loops, before they can be destroyed by the next cascade (see the video cascade-Ni.avi in the [supplementary material](#), starting at 0:40; defect close to the center of the box). As such, Ni possesses a higher

volume fraction of undisturbed lattice in which the net defect creation rate is always positive. Additionally, in contrast to the HEA, the stacking-fault tetrahedra are numerous.

In the final stage, we also observe a saturation of the defect concentration in pure Ni, while maintaining the steady state in the alloy system. The development of a steady state in the elemental structure is contrary to earlier publications,²⁰ where a continuous growth of defect networks has been detected. The reason for a reduced growth rate of defect concentrations in Ni is a simulation size effect,⁴⁷ since the earlier simulation used larger simulation cells compared to the current work.

In order to examine the stability of the lattice defects in the absence of irradiation, an MD simulation at 800 K for 1 ns was performed for the initially segregated HEA. The results reveal neither large movement nor creation or dissolution of a significant number of defects, which indicates that the defects are stable and sessile even at elevated temperatures (see video reanneal-irradiated-CuNiCoFe.avi in the [supplementary material](#)).

2. Chemical order

In the following, we analyze whether high energy recoils are able to initiate local segregation processes, or if the SRO remains more or less constant after every subsequent cascade. Again, we use the Warren-Cowley parameters $\alpha_{1,2}^{ij}$ for the first and second neighbor shell to quantify the extent of atomic clustering. Figure 5 shows $\alpha_{1,2}^{\text{Cu,Cu}}$ for two cells: the HEA with initially random atom distribution, and the HEA after MC/MD at 400 K which shows segregation tendencies for Cu. The analysis is limited to atoms in perfect FCC environments and therefore excludes atoms in defective sites introduced by the irradiation. Order parameters for pairs other than Cu–Cu are plotted in Fig. S1 in the [supplementary material](#). We find that the order parameter $\alpha_1^{\text{Cu,Cu}}$, although exhibiting initial partial segregation in the structure pre-ordered by MC/MD, eventually converges to small negative values. The initially random structure converges to the same value. A mid-range order is always disturbed by irradiation: the parameter $\alpha_2^{\text{Cu,Cu}}$ converges to zero in both cases. This shows that the cascade has two counteracting effects: First, it locally activates the thermodynamically preferable segregation of Cu. Second, it concurrently randomizes the element distribution. The resulting steady state is reached after approximately 700 cascades.

Figure 6 shows the comparison of the Warren-Cowley parameters $\alpha_{1,2}$ for all pairs in the CuNiCoFe alloy for both

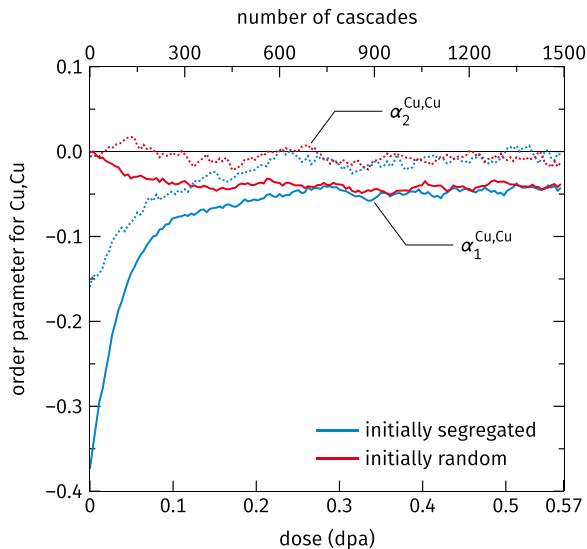


FIG. 5. Evolution of the SRO during irradiation. Only the Cu–Cu parameters are shown, the graphs for all parameters can be found in Fig. S1 in the [supplementary material](#). The sample which was equilibrated using VC-SGC (blue) and the one which was initially random (red) converge to the same values for the order parameters.

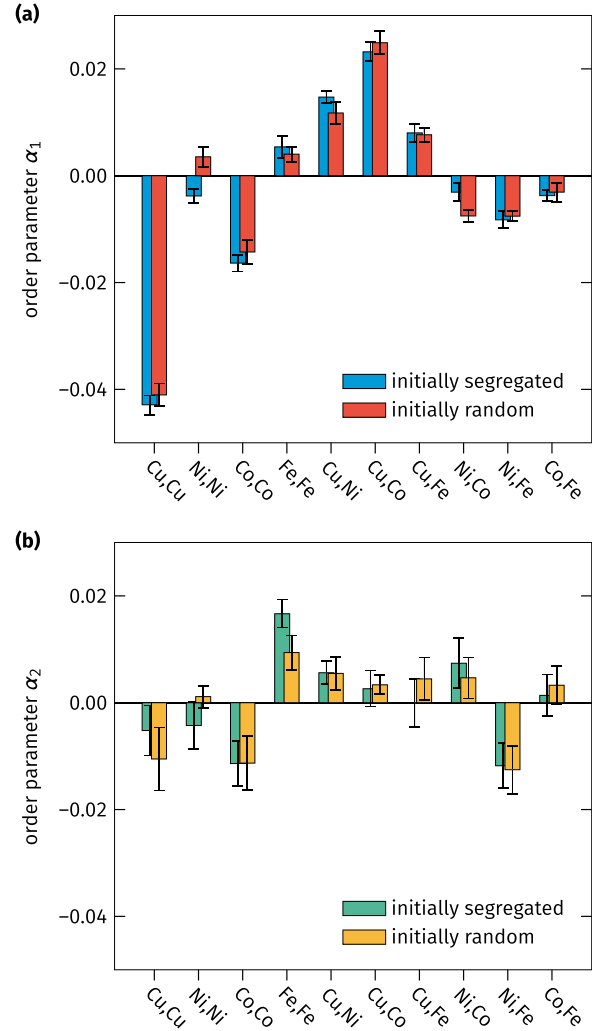


FIG. 6. Final order parameters for the first (a) and second neighbor shell (b) after irradiation with a dose of 0.57 dpa. The values are averaged over the last 10 frames of the irradiation simulation, with the error bars representing the standard deviation.

structures (pre-ordered and fully random) after the full irradiation dose. Comparing these results to those in Fig. 2 (note the scale difference in the y axes), we observe that the absolute values of both parameters α_1 and α_2 are reduced by roughly one order of magnitude due to the irradiation. Importantly, after irradiation all pairs have practically the same α parameters regardless of the initial state. We also note that the α_2 values are consistently smaller than the α_1 , indicating that the ordering effects under irradiation are limited to the nearest-neighbor shell.

Based on this analysis, we conclude that while collisional cascades provide activation energy for demixing, the system is dynamically driven to a mostly random steady state, independent of the initial chemical order.

IV. POST-IRRADIATION EFFECTS

Thermodynamic equilibration of a four-component CuNiCoFe alloy with a perfect FCC lattice showed a segregation tendency for Cu atoms. From the results of Sec. III A, we can assume that there is not only a chemical but also a steric driving force for Cu to segregate from the solid

solution into small clusters. We already concluded that the growth of Cu clusters is accompanied by an increasing Cu atomic volume. Nevertheless, thus far, we mainly concentrated on the thermodynamics of the defect-free system. Therefore, we again ran hybrid MC/MD simulations in the VC-SGC ensemble. However, this time, the irradiated sample with pre-existing defects was taken as a starting configuration. Table I lists the composition inside the lattice defects. Obviously, defect sites that offer excess volume serve as sinks for Cu atoms and even enhance the amount of segregated Cu after equilibration. In this regard, the presence of defects enhances the driving force for local decomposition. Within the defects, we can find a Cu proportion which is approximately 50%. In contrast, during the irradiation the distribution of Cu atoms does not alter significantly. In Fig. 7, we visualized the atoms located within the defect structure before (left) and after (right) the equilibration. Copper atoms are displayed with a red color, while all others are shown in gray. Figures 7(c) and 7(d) highlight two defects separately. From these illustrations, we draw the conclusion that Cu preferentially segregates on, e.g., the edges of stacking-fault tetrahedra rather than in the stacking faults themselves. The reason lies in the higher local excess volume of these sites (cf. Fig. 3).

In conclusion, all results suggest that the mixing enthalpy of Cu is the decisive factor for phase stability in this case, exceeding the total entropy with decreasing temperature. The limited segregation tendencies of the perfect crystal are surpassed in the presence of defects, which act as sinks for copper.

V. CONCLUSION

Using a model CuNiCoFe HEA with a tendency for copper segregation, we observe that the system reaches a steady state of defect concentration and of chemical order under irradiation, irrespective of the initial structure. In contrast to pure metals, irradiation leads to less mobile point defects and therefore a larger number of isolated defects instead of recombination or agglomeration. While, e.g., Ni increases its defect concentration continuously with increasing irradiation dose due to the agglomeration of defects in larger, more stable structures, the HEA quickly reaches a steady state of defect creation and annihilation. Irradiation provides the thermal activation for demixing of copper, but at the same

TABLE I. Composition inside defects of the irradiated sample before and after an additional, subsequent MC/MD run. Irradiated sample averaged over 50 snapshots (500 cascades). Note that the total composition of the sample stays equimolar during MC/MD because of the variance constraint and that the composition on the intact lattice sites also stays roughly equimolar because of the comparatively low amount of defect sites.

Element	Composition after irradiation (%)	Composition after subsequent MC/MD (%)
Cu	26.9	49.4
Ni	24.9	17.1
Co	23.3	14.0
Fe	24.9	19.5

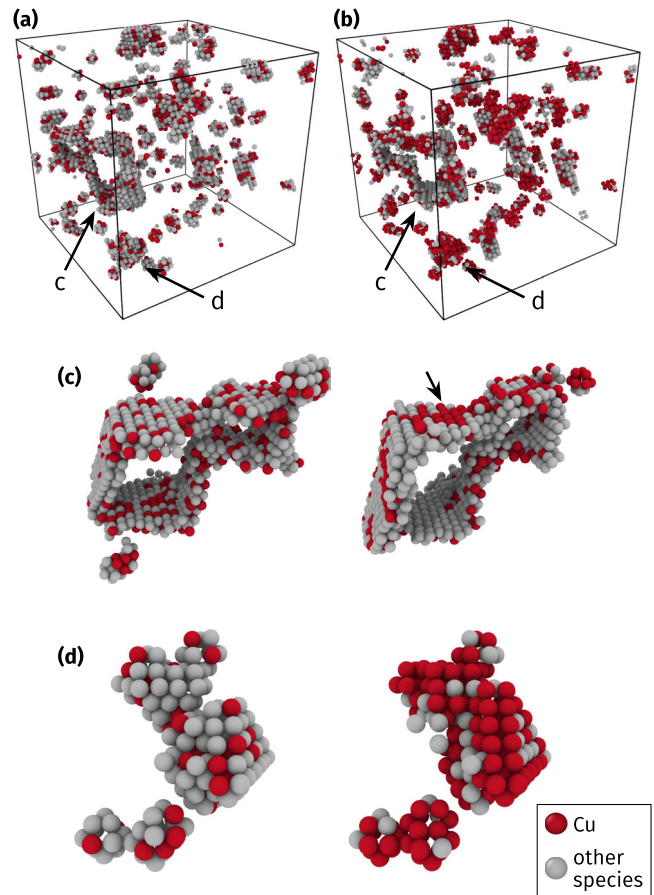


FIG. 7. VC-SGC simulations of the HEA sample after irradiation. (a) Atoms identified as defective by CNA after irradiation [same structure as the right-most snapshot in Fig. 4(a)]. Copper atoms are shown in red, all others in gray. (b) The same after subsequent simulation in the VC-SGC ensemble. The concentration of copper atoms around the defects is highly increased. Detailed views of a dislocation structure (c) and a stacking-fault tetrahedron (d) are provided.

time re-randomizes the elemental distribution. The resulting steady state of chemical order is close to a random solid solution, but still shows traces of local precipitation. Furthermore, our simulations reveal that various lattice defects act as sinks for copper, most likely since the copper atoms are the largest species and the defects provide excess volume. This clustering of copper at defects is also suppressed during irradiation for the reasons enumerated above. Together, these effects explain the high irradiation resistance of HEAs.

SUPPLEMENTARY MATERIAL

See [supplementary material](#) for videos of the irradiation simulations, a figure of the detailed evolution of SRO during irradiation, and additional data for the verification of the EAM potential.

ACKNOWLEDGMENTS

The authors gratefully acknowledge travel grants through the PPP Finland program of the Deutscher Akademischer Austauschdienst (DAAD) and K.A. acknowledges financial support by the Deutsche Forschungsgemeinschaft (DFG)

through project Grant No. STU 611/2-1. Computing time was made available by the Technische Universität Darmstadt on the Lichtenberg cluster and the IT Center for Science, CSC, Finland.

APPENDIX: VALIDATION OF THE EAM POTENTIAL

We used an EAM potential by Zhou *et al.*²⁴ for the Cu-Ni-Co-Fe system. This potential was tested for HEAs under driven conditions: Thin-film growth by sputtering yields comparable structures to experiment and the BCC to FCC transition is reproduced correctly.^{10,62} Furthermore, damage accumulation during irradiation agrees with data obtained by Rutherford backscattering spectrometry.³⁵

We performed additional validation of the potential by comparing the properties of the elements and of binary mixtures to reference values. In a first step, we produced FCC lattices of Cu, Ni, Co, and Fe, as well as HCP Co and BCC Fe. These were minimized to obtain the 0 K ground state values of the lattice constants a and c and the cohesive energy E_{coh} . The comparison to literature values in Table II reveals a good match. We then obtained the stiffness tensor using Hooke's law by calculating the stress tensors for finite deformations of the box at 1% strain. Apart from HCP cobalt, which does not occur in our samples, and FCC iron, which is too soft, the reference values are reproduced quite well. Using the procedure described in Ref. 55, we calculated the stacking fault energy γ_{SF} , the unstable stacking fault energy γ_{USF} , and the critical shear stress σ_{SF} for a stacking fault. While literature data contain large uncertainties and variations, the general trend of available data agrees with the predictions of the potential. As far as reference data are available, the same is true for the twinning faults, which we calculated

using the method described in Ref. 63. The negative values for the stacking and twinning faults in Co are of course the result of the lower energy of the stable HCP structure.

Furthermore, we calculated the elastic constants of those binary alloys, for which reference data are available, i.e., in the Fe-Co-Ni system. The results are presented in Table S.1 in the [supplementary material](#). Since the cross terms of the potential are obtained through a mixing procedure, the results match the expectations from the properties of the elements: The elastic constants match well, except for alloys containing FCC iron or HCP cobalt, which are too soft. To additionally determine the melting points of the elements and some miscible alloys, liquid-solid interface simulations were carried out.⁶⁴ A simulation cell of 2000 atoms was relaxed with the correct crystal structure and lattice constant, without pressure control. An equally sized box was molten and cooled down to the desired temperature, with pressure control in the z direction. The two boxes were then combined in the z direction, and were let to relax with pressure control in all directions. Below the melting point, the cell will solidify and the volume of the cell will decrease, while the opposite will happen above the melting point. Due to the chosen temperature stepping, an error of around 25 K is expected. The results are presented in Table S.2 in the [supplementary material](#) and show that the melting points slightly deviate from the reference values, but capture the features of the phase diagrams: For the pure elements, the deviation of the melting point is below 15% of the absolute value. The melting point of HCP cobalt agrees with the literature value within the expected error of the simulation. The melting points of the different binary subsystems studied are all within 10% of the expected value. We point out that a good description of the melting points is particularly important for

TABLE II. Comparison between the potential and literature values for properties of Cu, Ni, Co, and Fe. The table shows lattice constants a and c , the cohesive energy E_{coh} , the components of the stiffness tensor c_{ij} , the stacking fault energy γ_{SF} , the unstable stacking fault energy γ_{USF} , the critical shear stress σ_{SF} for a stacking fault, the twinning fault energy γ_{TF} , the unstable twinning fault energy γ_{UTF} , and the melting point T_{melt} .

	Cu (FCC)		Ni (FCC)		Co (FCC)		Co (HCP)		Fe (FCC)		Fe (BCC)	
	Pot.	Ref.	Pot.	Ref.	Pot.	Ref.	Pot.	Ref.	Pot.	Ref.	Pot.	Ref.
a (Å)	3.615	3.615 ⁴⁸	3.520	3.524 ⁴⁸	3.549	3.545 ⁴⁸	2.501	2.507 ⁴⁸	3.628	3.647 ⁴⁸	2.866	2.867 ⁴⁸
c (Å)							4.076	4.069 ⁴⁸				
c/a							1.630	1.623 ⁴⁸				
E_{coh} (eV/at.)	-3.54	-3.49 ⁴⁹	-4.45	-4.44 ⁴⁹	-4.40	-4.29 ^{a,50,51}	-4.41	-4.39 ⁴⁹	-4.20	-4.17 ⁵²	-4.29	-4.28 ⁴⁹
c_{11} (GPa)	170	168 ⁴⁸	246	248 ⁴⁸	213	225 ⁵³	263	307 ⁴⁸	107	154 ⁵⁴	229	226 ⁴⁸
c_{12} (GPa)	122	122 ⁴⁸	147	155 ⁴⁸	157	160 ⁵³	158	165 ⁴⁸	98	122 ⁵⁴	136	140 ⁴⁸
c_{13} (GPa)							124	103 ⁴⁸				
c_{33} (GPa)							363	358 ⁴⁸				
c_{44} (GPa)	76	76 ⁴⁸	125	124 ⁴⁸	99	92 ⁵³	65	76 ⁴⁸	80	77 ⁵⁴	117	116 ⁴⁸
γ_{SF} (mJ/m ²)	22	36-49 ⁵⁵⁻⁵⁷	97	133-183 ^{56,57}	-40							
γ_{USF} (mJ/m ²)	110	95-210 ^{b,55-57}	251	258 ⁵⁶	174							
σ_{SF} (GPa)	2.3	2.2 ⁵⁵	5.1		3.7							
γ_{TF} (mJ/m ²)	23		99		-44							
γ_{UTF} (mJ/m ²)	121	143 ⁵⁶	298	186 ⁵⁶	159							
T_{melt} (K)	1175	1357 ^{58,59}	1513	1728 ^{58,59}			1756	1768 ⁶⁰			2044	1811 ⁶¹

^aThere are considerably different absolute values reported in the literature. We assumed a difference of 0.1 eV/atom to the HCP structure, while the literature reports differences from 0.02 eV/atom to 0.15 eV/atom.

^bValue for Ref. 55 computed by numeric integration of the stress data.

the irradiation simulations, since several previous studies show that the outcome of molecular dynamics of collision cascades depends directly on the melting point.^{65,66}

In a next step, random solid solutions of all binary subsystems on FCC lattices were prepared. Additionally, if the binary alloy contained Fe or Co, BCC or HCP lattices, respectively, were created. Different molar fractions of each alloy and lattice type were minimized to obtain the mixing enthalpy

$$H_M = H_{AB} - (x_A H_A + x_B H_B), \quad (\text{A1})$$

where x_A , x_B , H_A , and H_B are the molar fractions and enthalpies of the constituents A and B, and where H_{AB} is the total enthalpy of the alloy. We included mixing enthalpy curves of all binary subsystems with respect to the concentration in Figs. S2–S7 in the [supplementary material](#) and compared them to literature values. We additionally compared our results to data from the THERMO-CALC software and database.^{67,68} In most cases, the EAM potential correctly describes the trend observed in the literature. However, it should be noted that even different literature values do not completely agree and that there is a large spread for some systems.

In order to get a clearer picture, we investigated the miscibility gaps of the binary subsystems. For this, equimolar alloys on FCC lattices were equilibrated in the semi-grand-canonical ensemble without a variance constraint. By systematically varying $\Delta\mu$, final compositions ranging over the whole phase diagram were obtained. The simulations were performed at 300 and 800 K. The concentration as a function of the chemical potential difference can be used to identify miscibility gaps in a binary subsystem: Given a dense mesh of $\Delta\mu_{A-B}$ values, miscibility gaps appear as discontinuities in the x_B ($\Delta\mu_{A-B}$) curves. Performing this analysis and comparing it to reference data showed that the potential is mostly able to reproduce phase diagram features, even though the miscibility is generally a bit too high. In the Co-containing systems, this method will not find the HCP phase, since the simulation setup was always initiated from an FCC structure. Due to the difference in the unit cell shape, the simulation suppresses the transition to HCP. We omit this investigation, since the HEA remains in the FCC structure in all conditions. The x_B ($\Delta\mu_{A-B}$) curves and a more detailed discussion of all binary subsystems can be found in Figs. S8–S13 in the [supplementary material](#).

Finally, the lattice constants of the binary systems were calculated from these simulations by time averaging the simulation cell volume of the different binary systems at 300 K. The data are shown in Table III and are in good agreement with experimental data. This confirms that the cross terms of the potential correctly predict the atomic volumes in alloys.

All in all, the potential performs reasonably well, reproducing the correct stable phases, densities, stiffnesses, and melting points. The limited data for stacking fault and twinning-fault energies suggest that lattice defects should be correctly reproduced. The main weakness of the potential is that the solubility of the alloys is too high in some cases, meaning that the tendencies for copper precipitation may be underestimated in the present work.

TABLE III. Lattice constants of binary random solid solutions at 300 K. The lattice structure is FCC unless stated otherwise.

	a (Å)	
	Pot.	Ref.
Cu ₃ Ni ₉₇	3.536	3.526 ^{69,70}
Cu ₄₉ Ni ₅₁	3.591	3.564 ^{69,70}
Cu ₉₅ Ni ₅	3.643	3.609 ^{69,70}
Cu ₈ Co ₉₂	3.568	3.551 ⁷¹
Cu ₂₁ Co ₇₉	3.607	3.577 ⁷¹
Cu ₈₆ Co ₁₄	3.636	3.668 ⁷¹
Cu ₉₉ Co ₁	3.646	3.674 ⁷¹
Cu ₂₃ Fe ₇₇ (BCC)	2.890	2.890 ⁷²
Cu ₉₆ Fe ₄	3.648	3.616 ⁷²
Ni ₂₆ Co ₇₄	3.555	3.539 ⁷³
Ni ₂₉ Co ₇₁	3.554	3.538 ⁷³
Ni ₄₉ Co ₅₁	3.548	3.533 ⁷³
Ni ₅₁ Co ₄₉	3.548	3.533 ⁷³
Ni ₇₂ Co ₂₈	3.541	3.528 ⁷³
Ni ₁₈ Fe ₈₂ (BCC)	2.869	2.867 ⁶¹
Ni ₃₉ Fe ₆₁	3.594	3.595 ⁶¹
Ni ₄₈ Fe ₅₂	3.584	3.590 ⁶¹
Ni ₄₉ Fe ₅₁	3.582	3.587 ⁶¹
Ni ₇₈ Fe ₂₂	3.552	3.552 ⁶¹
Co ₁₁ Fe ₈₉ (BCC)	2.869	2.861 ⁷⁴
Co ₂₄ Fe ₇₆	2.857	2.860 ⁷⁴

¹Z. Wang, S. Guo, and C. T. Liu, *JOM* **66**, 1966 (2014).

²Y. F. Ye, Q. Wang, J. Lu, C. T. Liu, and Y. Yang, *Mater. Today* **19**, 349 (2016).

³F. Otto, Y. Yang, H. Bei, and E. P. George, *Acta Mater.* **61**, 2628 (2013).

⁴E. J. Pickering and N. G. Jones, *Int. Mater. Rev.* **61**, 183 (2016).

⁵C. C. Tasan, Y. Deng, K. G. Pradeep, M. J. Yao, H. Springer, and D. Raabe, *JOM* **66**, 1993 (2014).

⁶J.-W. Yeh, *JOM* **65**, 1759 (2013).

⁷M. Widom, W. P. Huhn, S. Maiti, and W. Steurer, *Metall. Mater. Trans. A* **45**, 196 (2014).

⁸M.-H. Tsai and J.-W. Yeh, *Mater. Res. Lett.* **2**, 107 (2014).

⁹W. H. Liu, Y. Wu, J. Y. He, Y. Zhang, C. T. Liu, and Z. P. Lu, *JOM* **66**, 1973 (2014).

¹⁰L. Xie, P. Brault, J.-M. Bauchire, A.-L. Thomann, and L. Bedra, *J. Phys. D: Appl. Phys.* **47**, 224004 (2014).

¹¹F. Tian, L. K. Varga, N. Chen, L. Delczeg, and L. Vitos, *Phys. Rev. B* **87**, 075144 (2013).

¹²S.-W. Kao, J.-W. Yeh, and T.-S. Chin, *J. Phys: Condens. Matter* **20**, 145214 (2008).

¹³A. Haglund, M. Koehler, D. Catoor, E. P. George, and V. Keppens, *Intermetallics* **58**, 62 (2015).

¹⁴F. Tian, L. Delczeg, N. Chen, L. K. Varga, J. Shen, and L. Vitos, *Phys. Rev. B* **88**, 085128 (2013).

¹⁵S. Guo, Q. Hu, C. Ng, and C. T. Liu, *Intermetallics* **41**, 96 (2013).

¹⁶C. Ng, J. Luan, Q. Wang, S. Shi, and C. Liu, *J. Alloys Compd.* **584**, 530 (2014).

¹⁷T. Egami, W. Guo, P. D. Rack, and T. Nagase, *Metall. Mater. Trans. A* **45**, 180 (2014).

¹⁸Y. Zhang, G. M. Stocks, K. Jin, C. Lu, H. Bei, B. C. Sales, L. Wang, L. K. Béland, R. E. Stoller, G. D. Samolyuk, M. Caro, A. Caro, and W. J. Weber, *Nat. Commun.* **6**, 8736 (2015).

¹⁹F. Granberg, K. Nordlund, M. W. Ullah, K. Jin, C. Lu, H. Bei, L. M. Wang, F. Djurabekova, W. J. Weber, and Y. Zhang, *Phys. Rev. Lett.* **116**, 135504 (2016).

²⁰F. Granberg, F. Djurabekova, E. Levo, and K. Nordlund, *Nucl. Inst. Methods Phys. Res., Sect. B.* **393**, 114 (2017).

²¹T. Yang, S. Xia, S. Liu, C. Wang, S. Liu, Y. Fang, Y. Zhang, J. Xue, S. Yan, and Y. Wang, *Sci. Rep.* **6**, 32146 (2016).

²²M. W. Ullah, D. S. Aidhy, Y. Zhang, and W. J. Weber, *Acta Mater.* **109**, 17 (2016).

- ²³S. M. Foiles, M. I. Baskes, and M. S. Daw, *Phys. Rev. B* **33**, 7983 (1986).
- ²⁴X. W. Zhou, R. A. Johnson, and H. N. G. Wadley, *Phys. Rev. B* **69**, 144113 (2004).
- ²⁵K. T. Jacob, S. Raj, and L. Rannesh, *Int. J. Mater. Res.* **98**, 776 (2007).
- ²⁶S. Plimpton, *J. Comp. Phys.* **117**, 1 (1995).
- ²⁷B. Sadigh, P. Erhart, A. Stukowski, A. Caro, E. Martinez, and L. Zepeda-Ruiz, *Phys. Rev. B* **85**, 184203 (2012).
- ²⁸T. Brink, L. Koch, and K. Albe, *Phys. Rev. B* **94**, 224203 (2016).
- ²⁹K. Nordlund, *Parcas* computer code (2016). The main principles of the molecular dynamics algorithms are presented in Refs. [45](#) and [75](#). The adaptive time step and electronic stopping algorithms are the same as in Ref. [76](#). The 2016 version of the code is published in the online supplementary material to Ref. [19](#).
- ³⁰H. J. C. Berendsen, J. P. M. Postma, W. F. van Gunsteren, A. DiNola, and J. R. Haak, *J. Chem. Phys.* **81**, 3684 (1984).
- ³¹J. F. Ziegler, J. P. Biersack, and U. Littmark, *The Stopping and Range of Ions in Matter* (Pergamon, New York, 1985).
- ³²J. F. Ziegler, SRIM-96 computer code, private communication (1996).
- ³³ASTM Standard E693-94, *Standard Practice for Characterising Neutron Exposure in Iron and Low Alloy Steels in Terms of Displacements Per Atom (Dpa)* (ASTM International 1994).
- ³⁴K. Nordlund, S. J. Zinkle, T. Suzudo, R. S. Averback, A. Meinander, F. Granberg, L. Malerba, R. Stoller, F. Banhart, B. Weber, F. Willaime, S. Dudarev, and D. Simeone, *Primary Radiation Damage in Materials: Review of Current Understanding and Proposed New Standard Displacement Damage Model to Incorporate in-Cascade Mixing and Defect Production Efficiency Effects* (OECD Nuclear Energy Agency, Paris, France, 2015).
- ³⁵S. Zhang, K. Nordlund, F. Djurabekova, F. Granberg, Y. Zhang, and T. S. Wang, *Mater. Res. Lett.* **5**(6), 433–439 (2017).
- ³⁶J. M. Cowley, *Phys. Rev.* **77**, 669 (1950).
- ³⁷A. Stukowski, *Model. Simul. Mater. Sci. Eng.* **18**, 015012 (2010). <http://ovito.org/>.
- ³⁸G. Voronoï, *J. Reine Angew. Math.* **133**, 97 (1908).
- ³⁹G. Voronoï, *J. Reine Angew. Math.* **134**, 198 (1908).
- ⁴⁰G. Voronoï, *J. Reine Angew. Math.* **136**, 67 (1909).
- ⁴¹W. Brostow, M. Chybicki, R. Laskowski, and J. Rybicki, *Phys. Rev. B* **57**, 13448 (1998).
- ⁴²J. D. Honeycutt and H. C. Andersen, *J. Phys. Chem.* **91**, 4950 (1987).
- ⁴³A. Stukowski, *Model. Simul. Mater. Sci. Eng.* **20**, 045021 (2012).
- ⁴⁴A. Stukowski, V. V. Bulatov, and A. Arsenlis, *Model. Simul. Mater. Sci. Eng.* **20**, 085007 (2012).
- ⁴⁵K. Nordlund, M. Ghaly, R. S. Averback, M. Caturia, T. Diaz de la Rubia, and J. Tarus, *Phys. Rev. B* **57**, 7556 (1998).
- ⁴⁶K. Nordlund and F. Gao, *Appl. Phys. Lett.* **74**, 2720 (1999).
- ⁴⁷E. Levo, F. Granberg, C. Fridlund, K. Nordlund, and F. Djurabekova, *J. Nucl. Mater.* **490**, 323 (2017).
- ⁴⁸*CRC Handbook of Chemistry and Physics*, 84th ed., edited by D. R. Lide (CRC Press, Boca Raton, Florida, USA, 2003).
- ⁴⁹C. Kittel, *Introduction to Solid State Physics*, 8th ed. (John Wiley & Sons, Inc., 2005).
- ⁵⁰F. Cardellini and G. Mazzone, *Philos. Mag. A* **67**, 1289 (1993).
- ⁵¹V. A. de la Peña O'Shea, I. de, P. R. Moreira, A. Roldán, and F. Illas, *J. Chem. Phys.* **133**, 024701 (2010).
- ⁵²M. Müller, P. Erhart, and K. Albe, *J. Phys.: Condens. Matter* **19**, 326220 (2007).
- ⁵³J. Gump, H. Xia, M. Chirita, R. Sooryakumar, M. A. Tomaz, and G. R. Harp, *J. Appl. Phys.* **86**, 6005 (1999).
- ⁵⁴J. Zarestky and C. Stassis, *Phys. Rev. B* **35**, 4500 (1987).
- ⁵⁵S. Ogata, J. Li, and S. Yip, *Science* **298**, 807 (2002).
- ⁵⁶Z.-H. Jin, P. Gumbsch, K. Albe, E. Ma, K. Lu, H. Gleiter, and H. Hahn, *Acta Mater.* **56**, 1126 (2008).
- ⁵⁷J. A. Zimmerman, H. Gao, and F. F. Abraham, *Model. Simul. Mater. Sci. Eng.* **8**, 103 (2000).
- ⁵⁸D. J. Chakrabarti, D. E. Laughlin, S. W. Chen, and Y. A. Chang, *Phase Diagrams of Binary Nickel Alloys* (ASM, Metals Park, OH, USA, 1991), Chap. Cu–Ni (Copper–Nickel), pp. 85–95.
- ⁵⁹D. J. Chakrabarti, D. E. Laughlin, S. W. Chen, and Y. A. Chang, *Phase Diagrams of Binary Copper Alloys* (ASM International, Materials Park, OH, USA, 1994), Chap. Cu–Ni (Copper–Nickel), pp. 266–270.
- ⁶⁰T. Nishizawa and K. Ishida, *Bull. Alloy Phase Diagrams* **5**, 161 (1984).
- ⁶¹L. J. Swartzendruber, V. P. Itkin, and C. B. Alcock, *J. Phase Equilib.* **12**, 288 (1991).
- ⁶²L. Xie, P. Brault, A.-L. Thomann, and J.-M. Bauchire, *Appl. Surf. Sci.* **285**(Part B), 810 (2013).
- ⁶³E. B. Tadmor and S. Hai, *J. Mech. Phys. Solids* **51**, 765 (2003).
- ⁶⁴F. Ercolessi, O. Tomagnini, S. Iarlori, and E. Tosatti, “Molecular dynamics simulations of metal surfaces,” in *Nanosources and Manipulation of Atoms Under High Fields and Temperatures: Applications* (Kluwer, Dordrecht, Netherlands, 1993), pp. 185–205.
- ⁶⁵K. Nordlund, L. Wei, Y. Zhong, and R. S. Averback, *Phys. Rev. B* **57**, R13965(R) (1998).
- ⁶⁶K. Nordlund, K. O. E. Henriksson, and J. Keinonen, *Appl. Phys. Lett.* **79**, 3624 (2001).
- ⁶⁷Thermo-Calc Software, <http://www.thermocalc.com> for TC Binary Solutions Database, Version 1.0; accessed 26 July 2017.
- ⁶⁸J. O. Andersson, T. Helander, L. Höglund, P. Shi, and B. Sundman, *Calphad* **26**, 273 (2002).
- ⁶⁹B. R. Coles, *J. Inst. Met.* **84**, 346 (1956).
- ⁷⁰J. K. A. Clarke and T. A. Spooner, *J. Phys. D: Appl. Phys.* **4**, 1196 (1971).
- ⁷¹B. Predel, *Landolt–Börnstein—Group IV Physical Chemistry Volume 5C: Ca–cd – co–zr* (Springer-Verlag, Berlin/Heidelberg, 1993), Chap. Co–Cu (Cobalt–Copper).
- ⁷²W. Klement, *Trans Metall Soc. AIME* **233**, 1180 (1965).
- ⁷³T. Nishizawa, S. Hao, M. Hasebe, and K. Ishida, *Acta Metall.* **31**, 1403 (1983).
- ⁷⁴W. Ellis and E. Greiner, *Trans. ASM* **29**, 415 (1941).
- ⁷⁵M. Ghaly, K. Nordlund, and R. S. Averback, *Philos. Mag. A* **79**, 795 (1999).
- ⁷⁶K. Nordlund, *Comput. Mater. Sci.* **3**, 448 (1995).

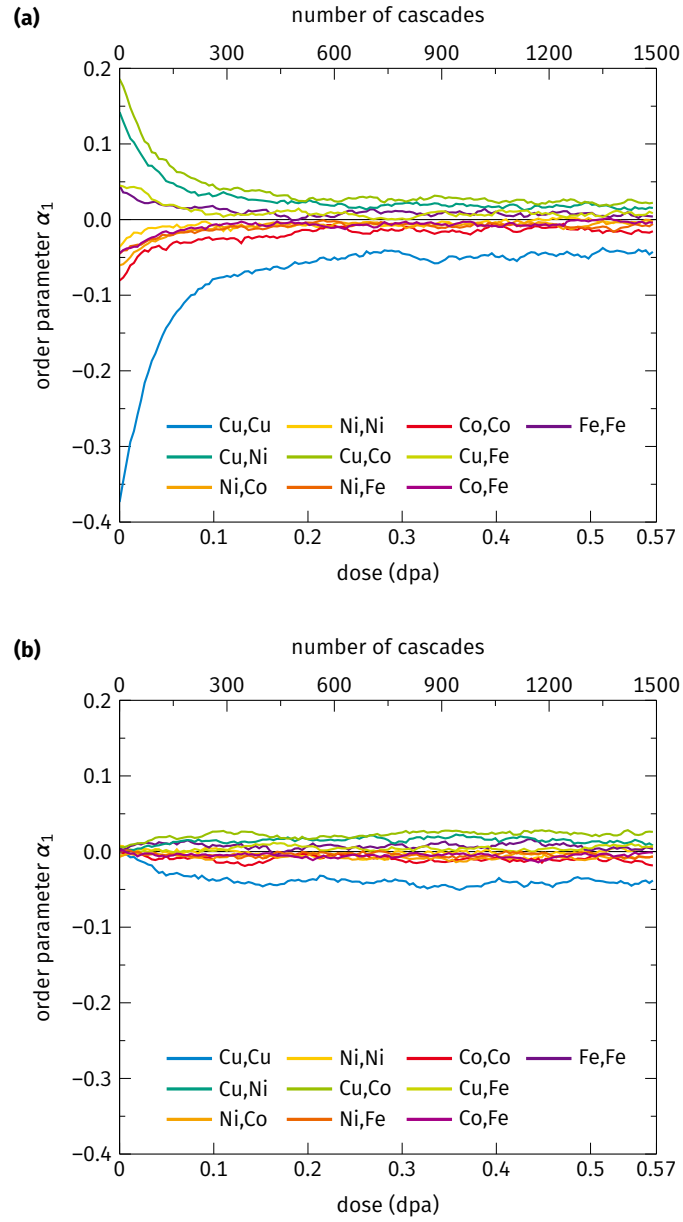


Figure S.1: Evolution of the SRO in CuNiCoFe HEAs during irradiation for all pairs (cf. Fig. 5 in the main paper). (a) Starting from the ordered sample (MC/MD at 400 K). (b) Starting from the initially random sample.

Table S.1: Elastic constants of binary alloys. FCC and HCP represent random solid solutions on these lattices. B2 represents an ordered CsCl structure. The stiffness tensor c_{ij} , the bulk modulus K , the shear modulus G , and the Young’s modulus Y are listed. For the shear and Young’s moduli, we assumed that the reference is for a polycrystalline sample. Thus, we calculated the Voigt–Reuss–Hill (VRH) average from the stiffness tensor.^{1–3}

	c_{11} (GPa)		c_{12} (GPa)		c_{13} (GPa)		c_{33} (GPa)		c_{44} (GPa)		K (GPa)		G_{VRH} (GPa)		Y_{VRH} (GPa)	
	Pot.	Ref.	Pot.	Ref.	Pot.	Ref.	Pot.	Ref.	Pot.	Ref.	Pot.	Ref.	Pot.	Ref.	Pot.	Ref.
Co ₅₀ Ni ₅₀ (FCC)	231		153						113		179	257 ^{4,a}	74		194	
Co ₆₈ Ni ₃₂ (FCC)	225	239 ⁵	155	155 ⁵					108	132 ⁵						
Co ₆₈ Ni ₃₂ (HCP)	278	326 ⁵	153	161 ⁵	108		323	358 ⁵	61	74 ⁵						
Fe ₃₀ Ni ₇₀ (FCC)	194	233 ⁶	138	146 ⁶					117	127 ⁶	156		67	78 ⁶	175	206 ⁶
Fe ₅₀ Ni ₅₀ (FCC)	164	200 ⁶	130	142 ⁶					108	107 ⁶	142		53	64 ⁶	141	171 ⁶
Fe ₆₅ Ni ₃₅ (FCC)	149	215 ⁷	129	175 ⁷					100		136	188 ⁷	43	57–59 ⁶	117	145–151 ⁶
Fe ₇₀ Ni ₃₀ (FCC)	144	146 ⁶	127	88 ⁶					98	113 ⁶	133	110;180 ^{8,b}	40	65 ⁶	110	161 ⁶
FeCo (B2)	222		171						129		188	247 ^{9,c}	69		183	

^a The authors of Ref. 4 (a DFT calculation) note that the stiffness of pure Ni lies around 40% higher than the available experimental data. If we assume that the same is true for the binary alloy, the resulting value of $K = 184$ GPa compares favorably to the potential.

^b The lower value corresponds to the ferromagnetic, the higher value to the paramagnetic phase.

^c The DFT calculations in Ref. 9 again overestimate the stiffness of pure Fe by around 40%. Correcting the value for FeCo by the same percentage yields $K = 176$ GPa, which is in good agreement with the potential.

Table S.2: Melting points T_{melt} of the elements and the miscible binary alloys.

	T_{melt} (K)	
	Pot.	Ref.
Ni	1513	1728 ^{10,11}
Cu	1175	1357 ^{10,11}
Fe	2044	1811 ¹²
Co	1756	1768 ¹³
NiCo	1625	1748 ¹³
NiFe	1656	1718 ¹²
Ni ₂ Fe	1594	1713 ¹²
Ni ₃ Fe	1582	1714 ¹²

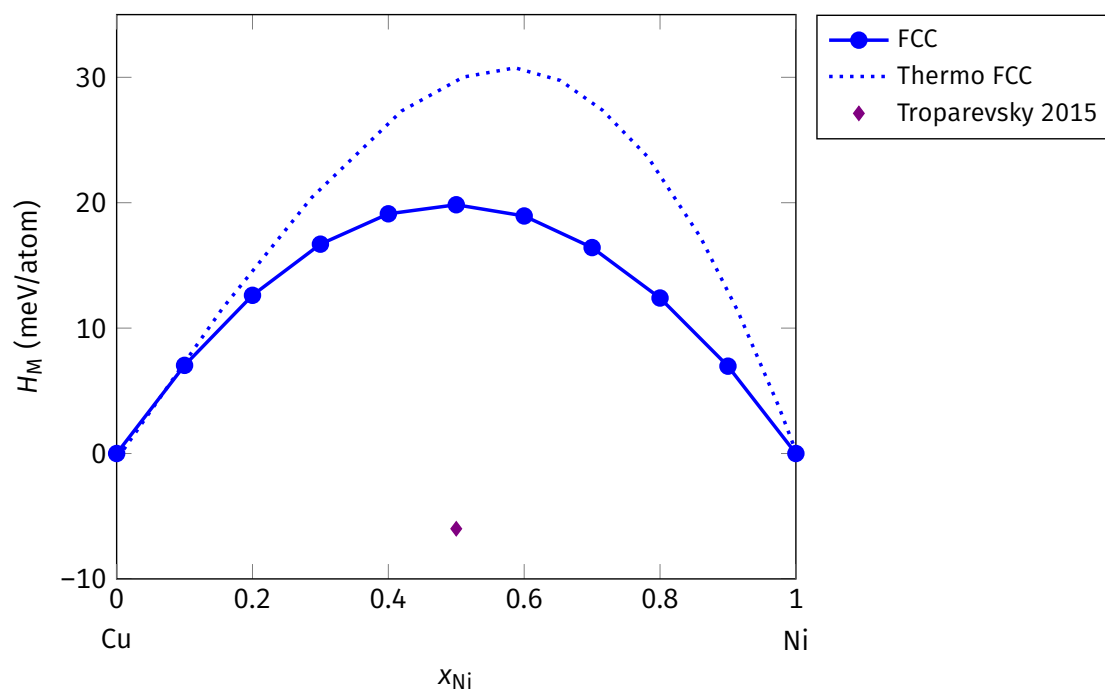


Figure S.2: Mixing enthalpy of a Cu–Ni binary subsystem with an FCC (blue dots) lattice structure. We found reference data in Troparevsky 2015¹⁴ (violet diamonds) for an equimolar alloy system. The obtained mixing enthalpy shows a large deviation from our results. Enthalpy data obtained from the THERMO-CALC software^{15,16} (dotted blue line), on the other hand, shows a similar trend compared to the present EAM potential.

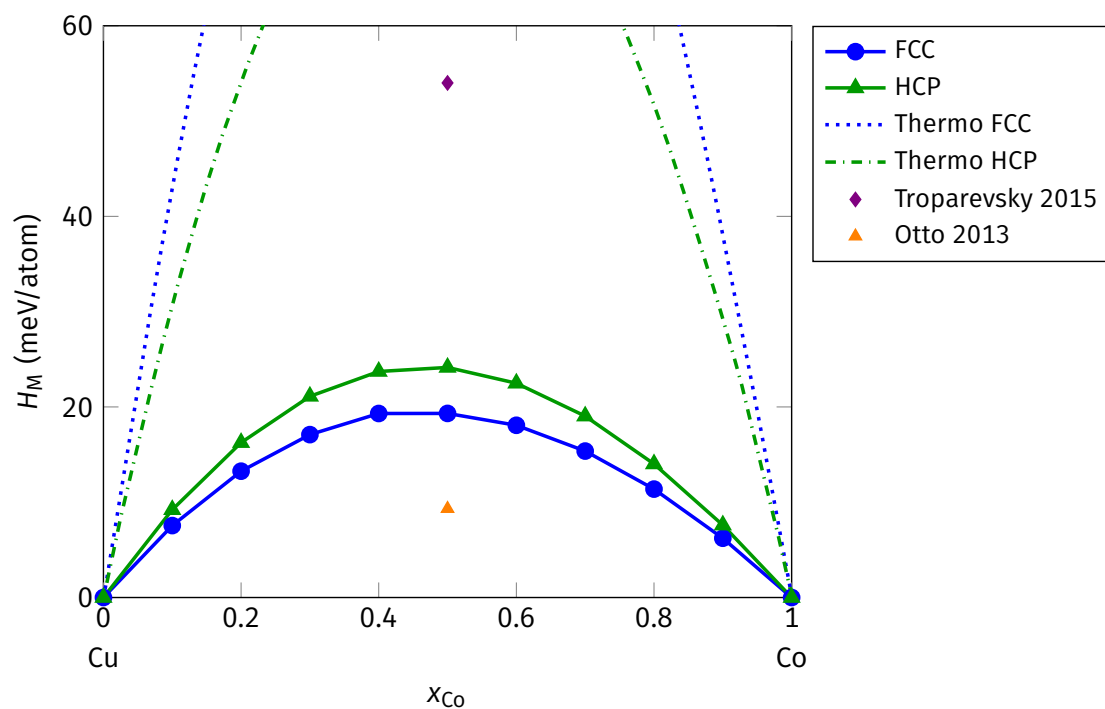


Figure S.3: Mixing enthalpies of Cu–Co binary subsystems with FCC (blue dots) and with HCP (green triangles) lattice structures. Reference data from Otto 2013¹⁷ (orange triangles) roughly agrees with the potential, while both Troparevsky 2015¹⁴ (violet diamonds) and THERMO-CALC^{15,16} (dotted blue line and dash-dotted green line) specify much higher values.

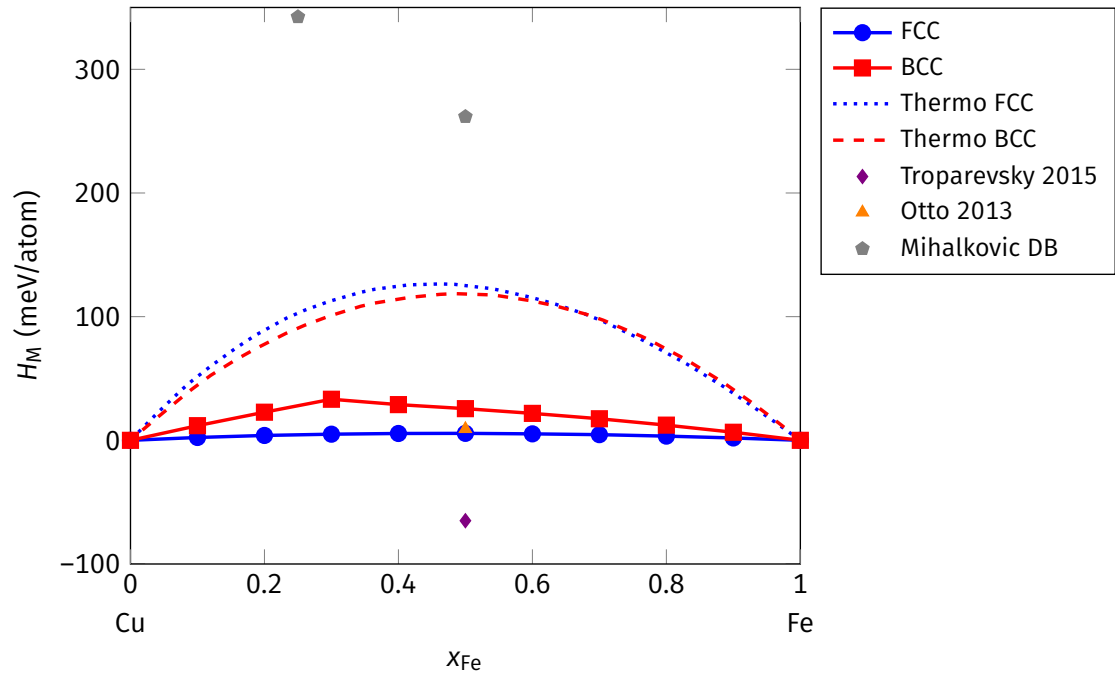


Figure S.4: Mixing enthalpies of Cu–Fe binary subsystems with FCC (blue dots) and with BCC (red squares) lattice structures. We compared our mixing enthalpies with Otto 2013¹⁷ (orange triangles), Troparevsky 2015¹⁴ (violet diamonds), the Mihalkovic database¹⁸ (gray pentagons), and the THERMO-CALC database^{15,16} (dotted blue line and dashed red line). In this subsystem, too, the value of Otto 2013 fits best with the results of the present study. In this case, the huge spread of the reference data becomes particularly apparent.

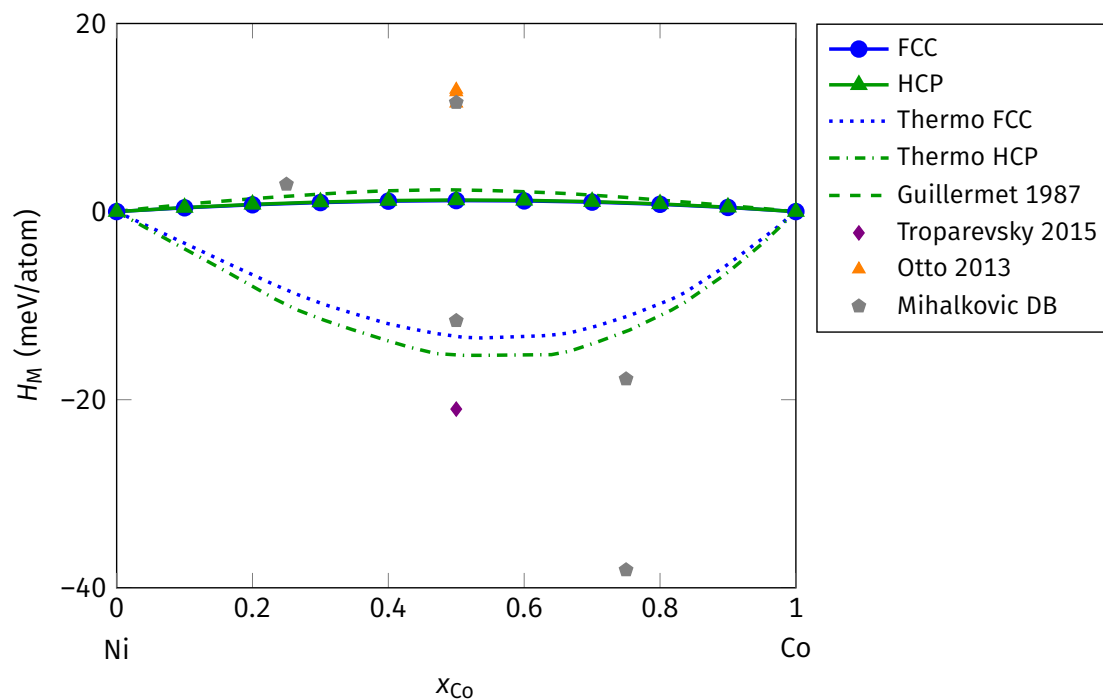


Figure S.5: Mixing enthalpies of Ni–Co binary subsystems with FCC (blue dots) and HCP (green triangles) lattice structures, both of which exhibit the same mixing enthalpies. We compared our findings with the data of Otto 2013¹⁷ (orange triangles), Troparevsky 2015¹⁴ (violet diamonds), Guillermet 1987¹⁹ (green dashed line), the Mihalkovic database¹⁸ (gray pentagons), and the THERMOCALC database^{15,16} (dotted blue line and dash-dotted green line). It can be seen that the agreement with the reference values depends on the composition. Here, the values of Guillermet 1987 almost coincide with our data. All other reference data strongly differ, some even by their sign. It should be noted that the positive mixing enthalpies of the EAM potential are so small that the resulting systems are still miscible at room temperature, as expected from experiment.

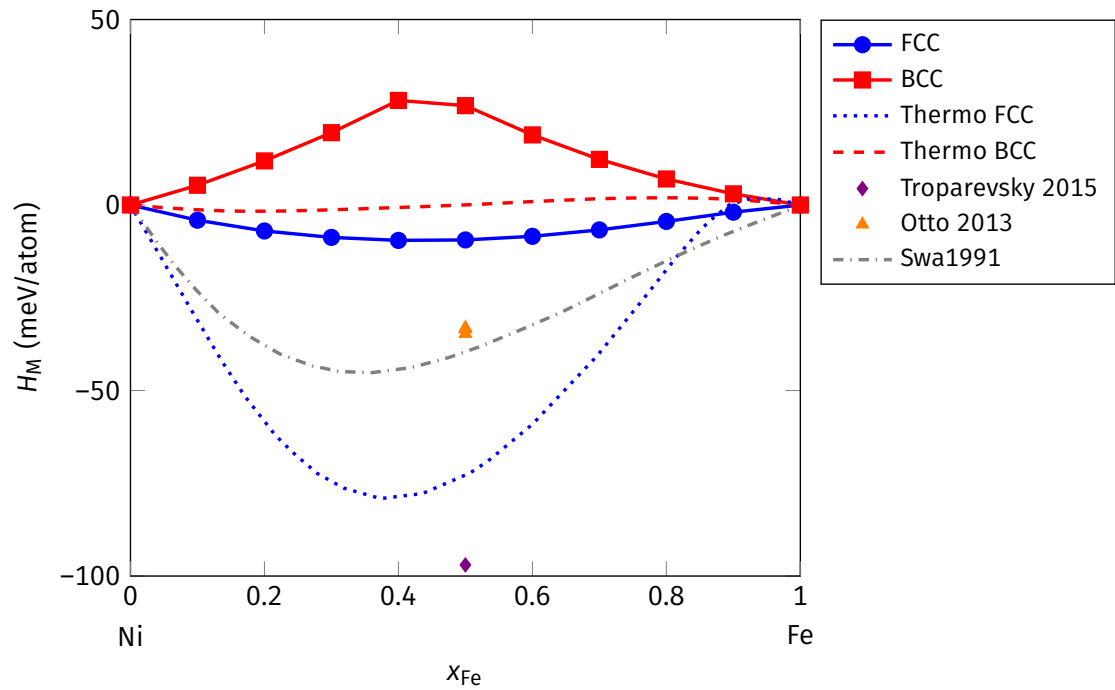


Figure S.6: Mixing enthalpies of Ni–Fe subsystems with FCC (blue dots) and BCC (red squares) lattice structures. As a reference, we included data from Swartzendruber 1991¹² (gray dashed line), Otto 2013¹⁷ (orange triangles), Troparevsky 2015¹⁴ (violet diamonds), and the THERMO-CALC database^{15,16} (dotted blue line and dashed red line). Again, the absolute values in this subsystem are not comparable. Nevertheless, the right trend is obtained: The system is miscible.

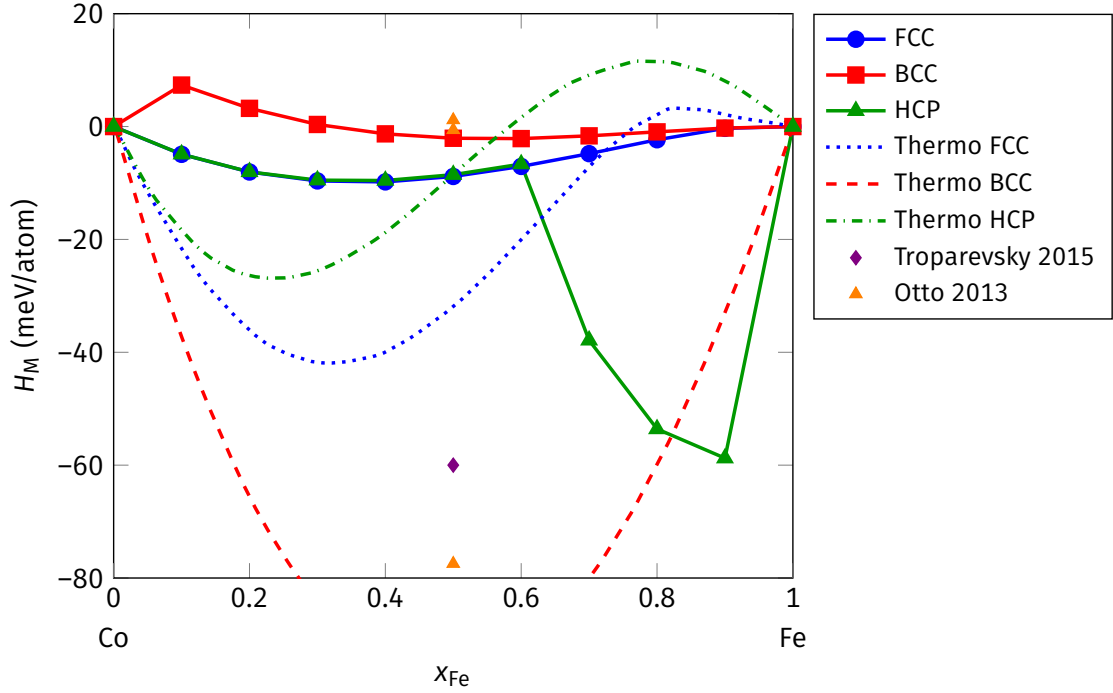


Figure S.7: Mixing enthalpy of Co–Fe binary subsystems with FCC (blue dots), HCP (green triangles), and BCC (red squares) lattice structures. We included reference data from Otto 2013¹⁷ (orange triangles) and Troparevsky 2015¹⁴ (violet diamonds) for an equimolar alloy. The data from THERMO-CALC^{15,16} (dotted blue line, dashed red line, and dash-dotted green line) deviates strongly from the potential and the other references in this case. Again, the reference data from Otto 2013 almost coincides with our calculations. The system is miscible, as expected from the phase diagram.²⁰ The anomalous decrease in mixing enthalpies for the simulated, iron-rich HCP structure describes a thermodynamically unstable state. It does not occur in the present work, which is concerned with FCC HEAs.

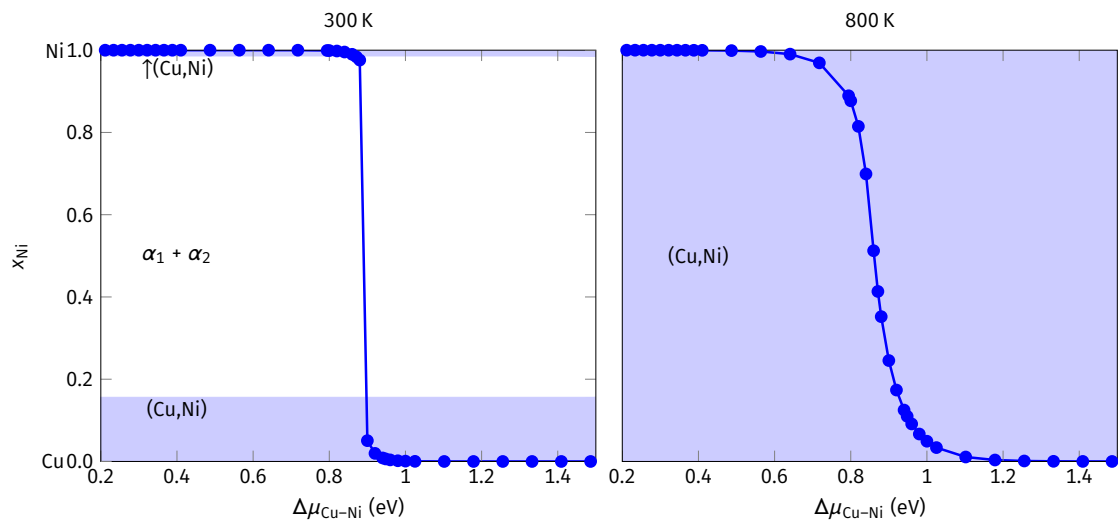


Figure S.8: Molar fraction of Ni in the Cu–Ni binary subsystem as a function of the chemical potential difference $\Delta\mu$ at 300 K and 800 K. Shaded areas indicate phases extracted and extrapolated from Chakrabarti *et al.*,^{10,11} while white areas are miscibility gaps. At 300 K the miscibility is slightly too low, leading to an overly large miscibility gap (indicated by an absence of data points). An FCC solid solution is observed over the whole compositional range at 800 K, in accordance with the reference phase diagram.

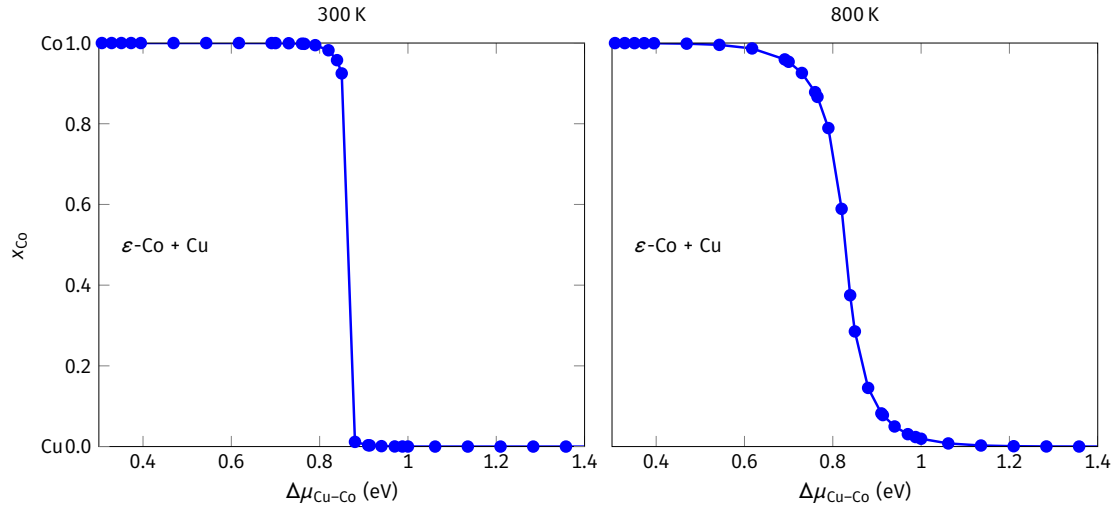


Figure S.9: Molar fraction of Co in the Cu–Co binary subsystem as a function of the chemical potential difference $\Delta\mu$ at 300 K and 800 K. From Nishizawa *et al.*¹³ it can be seen that Cu–Co only shows insignificant miscibility at 300 K and 800 K. While this is almost reproduced at 300 K with only a slight miscibility of Cu in Co, at 800 K, miscibility is observed over the whole compositional range. Due to the simulation setup, transitions from FCC to HCP cannot be observed, which leads to an FCC solid solution at all concentrations. Possibly, a phase separation into Cu (FCC) and ϵ -Co (HCP) may be more stable than the FCC solid solution and recover the phase diagram qualitatively. In HEAs, though, cobalt is not known to precipitate in an HCP phase.

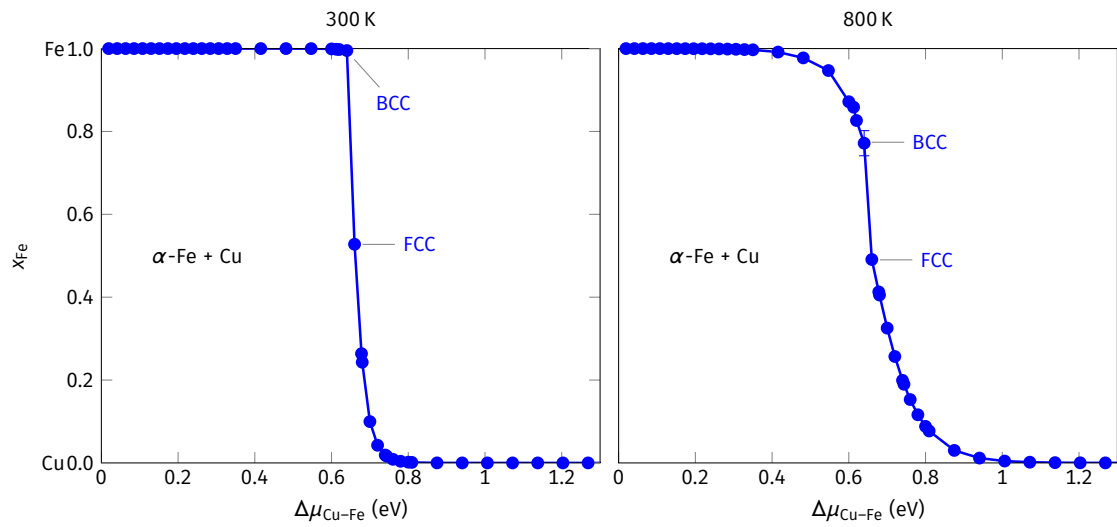


Figure S.10: Molar fraction of Cu in the Cu–Fe binary subsystem as a function of the chemical potential difference $\Delta\mu$ at 300 K and 800 K. From Ansara *et al.*²¹ it can be seen that Cu–Fe only shows insignificant miscibility at 300 K and 800 K. An FCC to BCC transition is observed; arrows indicate the last BCC and first FCC structures in the simulation. At both given temperatures, the simulation exaggerates the miscibility of Cu and Fe significantly, especially on FCC lattices.

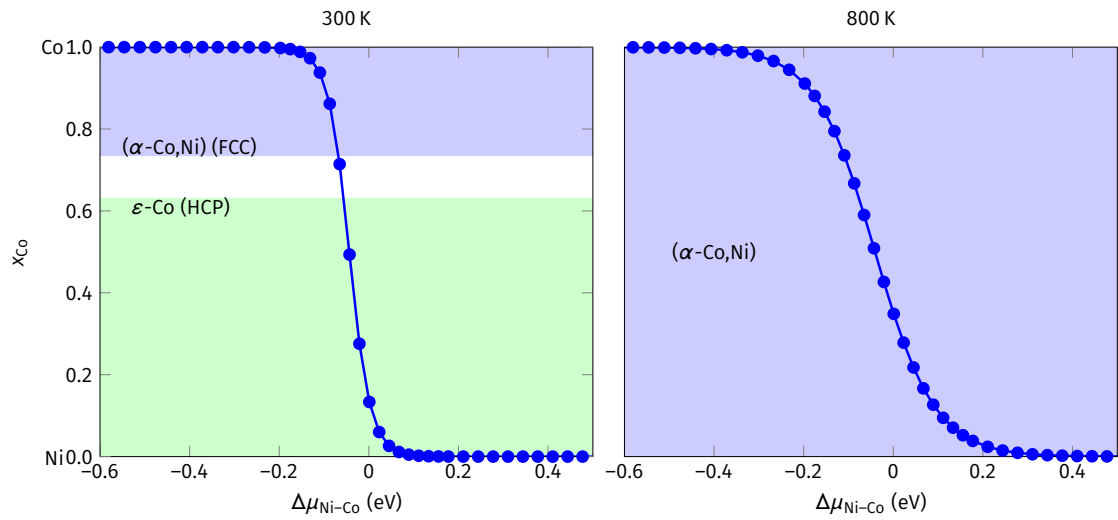


Figure S.11: Molar fraction of Co in the Ni–Co binary subsystem as a function of the chemical potential difference $\Delta\mu$ at 300 K and 800 K. Shaded areas indicate phases extracted and extrapolated from Nishizawa *et al.*²² Due to constraints in the simulation setup, HCP phases do not occur. Therefore, an FCC solid solution is observed over the whole compositional range. The inability to transition from FCC to HCP renders us unable to observe the small miscibility gap at 300 K, similar to Fig. S.9. At 800 K the phase diagram is reproduced.

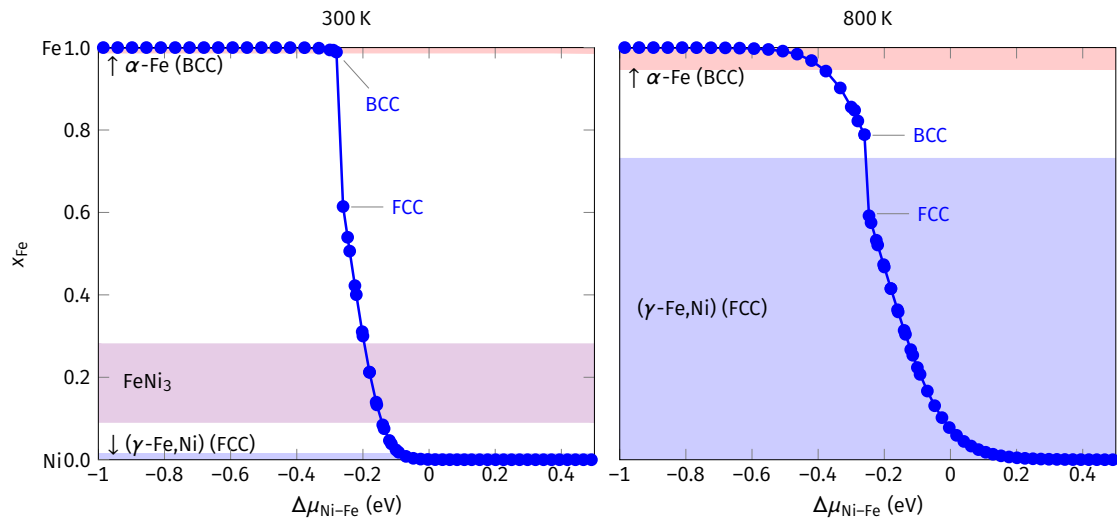


Figure S.12: Molar fraction of Fe in the Ni–Fe binary subsystem as a function of the chemical potential difference $\Delta\mu$ at 300 K and 800 K. Shaded areas indicate phases extracted and partially extrapolated from Swartzendruber *et al.*¹² The miscibility gap (indicated by an absence of data points) is underrepresented at 300 K. It should be noted, though, that FeNi_3 is an $L1_2$ phase, an ordered phase on an FCC lattice. Thus, while the potential does not capture the ordered phase, the extended FCC miscibility coincides with the $L1_2$ phase. At 800 K, the miscibility gap is shifted to lower concentrations. Arrows indicate the last BCC and first FCC structures observed in our simulations.

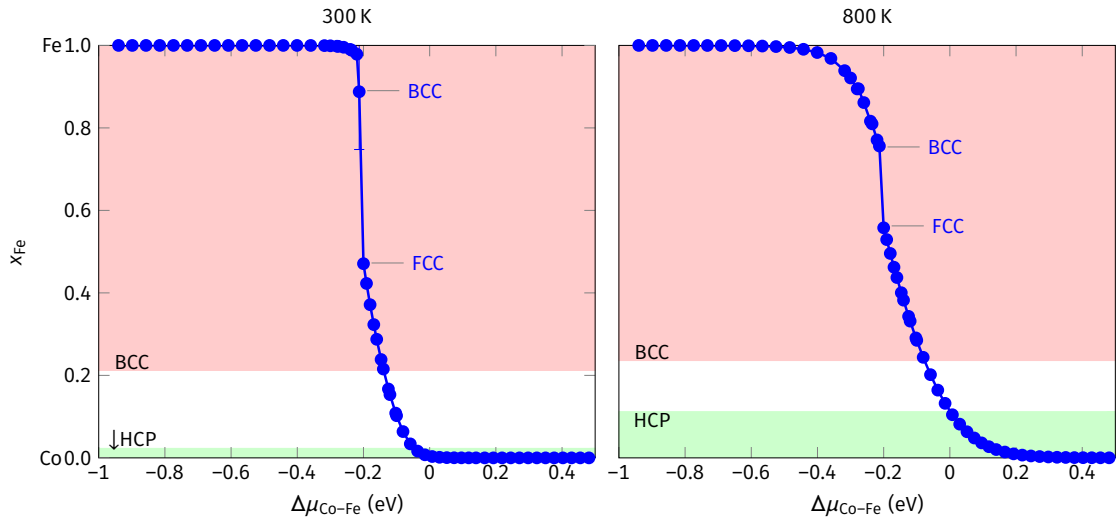


Figure S.13: Molar fraction of Fe in the Co–Fe binary subsystem as a function of the chemical potential difference $\Delta\mu$ at 300 K and 800 K. Shaded areas indicate phases extracted from Guillermet.²⁰ Due to constraints in the simulation setup, HCP phases do not occur. Therefore, an FCC to BCC transition is observed. The absence of HCP phases does not allow for a comparison of the miscibility gap (indicated by an absence of data points) with the phase diagram. At 800 K, the range of the miscibility gap is matched well, but it is strongly shifted to higher Fe concentrations. Arrows indicate the last BCC and first FCC structures observed in our simulations.

References

- [1] W. Voigt, *Lehrbuch der Kristallphysik*, Teubner, 1928.
- [2] A. Reuss, *Berechnung der Fließgrenze von Mischkristallen auf Grund der Plastizitätsbedingung für Einkristalle*, ZAMM **9**, 49–58 (1929).
- [3] R. Hill, *The elastic behaviour of a crystalline aggregate*, Proc. Phys. Soc. A **65**, 349 (1952).
- [4] A. B. Shick, V. Drchal, J. Kudrnovský, and P. Weinberger, *Electronic structure and magnetic properties of random alloys: Fully relativistic spin-polarized linear muffin-tin-orbital method*, Phys. Rev. B **54**, 1610–1621 (1996).
- [5] W. F. Weston and A. V. Granato, *Cubic and hexagonal single-crystal elastic constants of a cobalt-nickel alloy*, Phys. Rev. B **12**, 5355–5362 (1975).
- [6] D. Bonnenberg, K. A. Hempel, and H. P. J. Wijn, *Landolt-Börnstein – Group III Condensed Matter · Volume 19A: 3d, 4d and 5d Elements, Alloys and Compounds*, ch. 1.2.1.2.9 Magnetomechanical properties, elastic moduli, sound velocity, pp. 233–244, Springer-Verlag Berlin Heidelberg, 1986.
- [7] Y. Endoh and Y. Noda, *Zero sound anomaly in a ferromagnetic Invar alloy $Fe_{65}Ni_{35}$* , J. Phys. Soc. Jpn. **46**, 806–814 (1979).
- [8] G. Oomi and N. Mori, *High pressure x-ray study of anomalous bulk modulus of an $Fe_{70}Ni_{30}$ Invar alloy*, J. Phys. Soc. Jpn. **50**, 1043–1044 (1981).
- [9] A. Y. Liu and D. J. Singh, *General-potential study of the electronic and magnetic structure of $FeCo$* , Phys. Rev. B **46**, 11145–11148 (1992).
- [10] D. J. Chakrabarti, D. E. Laughlin, S. W. Chen, and Y. A. Chang, *Phase diagrams of binary nickel alloys*, ch. Cu–Ni (Copper–Nickel), pp. 85–95, ASM, Metals Park, OH, USA, 1991.
- [11] D. J. Chakrabarti, D. E. Laughlin, S. W. Chen, and Y. A. Chang, *Phase diagrams of binary copper alloys*, ch. Cu–Ni (Copper–Nickel), pp. 266–270, ASM International, Materials Park, OH, USA, 1994.
- [12] L. J. Swartzendruber, V. P. Itkin, and C. B. Alcock, *The Fe–Ni (iron–nickel) system*, J. Phase Equilib. **12**, 288–312 (1991).
- [13] T. Nishizawa and K. Ishida, *The Co–Cu (cobalt–copper) system*, Bull. Alloy Phase Diagrams **5**, 161–165 (1984).
- [14] M. C. Tropicovsky, J. R. Morris, P. R. C. Kent, A. R. Lupini, and G. M. Stocks, *Criteria for predicting the formation of single-phase high-entropy alloys*, Phys. Rev. X **5**, 011041 (2015).

- [15] Thermo-Calc Software, TC Binary Solutions Database, Version 1.0, <http://www.thermocalc.com/> (accessed 26 July 2017).
- [16] J. O. Andersson, T. Helander, L. Höglund, S. P. F., and B. Sundman, *Thermo-Calc and DICTRA, computational tools for materials science*, Calphad **26**, 273–312 (2002).
- [17] F. Otto, Y. Yang, H. Bei, and E. P. George, *Relative effects of enthalpy and entropy on the phase stability of equiatomic high-entropy alloys*, Acta Mater. **61**, 2628–2638 (2013).
- [18] Density-functional calculations performed by Mihalkovic, Widom, *et al.*, <http://alloy.phys.cmu.edu>.
- [19] F. Guillermet, *Assessment of the thermodynamic properties of the Ni–Co system*, Z. Metallkd. **78**, 639–647 (1987).
- [20] A. F. Guillermet, *Thermodynamic properties of the Fe–Co–C system*, Z. Metallkd. **79**, 317–329 (1988).
- [21] I. Ansara, A. T. Dinsdale, and M. H. Rand, *COST 507: Definition of thermochemical and thermophysical properties to provide a database for the development of new light alloys*, vol. 2, EUR-OP, Luxembourg, 1998.
- [22] T. Nishizawa and K. Ishida, *The Co–Ni (cobalt–nickel) system*, Bull. Alloy Phase Diagrams **4**, 390–395 (1983).